
Research Article: New Research | Sensory and Motor Systems

Predicting neural response latency of the human early visual cortex from MRI-based tissue measurements of the optic radiation

<https://doi.org/10.1523/ENEURO.0545-19.2020>

Cite as: eNeuro 2020; 10.1523/ENEURO.0545-19.2020

Received: 19 December 2019

Revised: 7 May 2020

Accepted: 12 May 2020

This Early Release article has been peer-reviewed and accepted, but has not been through the composition and copyediting processes. The final version may differ slightly in style or formatting and will contain links to any extended data.

Alerts: Sign up at www.eneuro.org/alerts to receive customized email alerts when the fully formatted version of this article is published.

Copyright © 2020 Takemura et al.

This is an open-access article distributed under the terms of the Creative Commons Attribution 4.0 International license, which permits unrestricted use, distribution and reproduction in any medium provided that the original work is properly attributed.

1 **1. Title:** Predicting neural response latency of the human early visual cortex from
2 MRI-based tissue measurements of the optic radiation

3 **2. Abbreviated Title:** Latency prediction from white matter properties

4 **3. Authors:** Hiromasa Takemura^{1,2)}, Kenichi Yuasa^{1,3)}, Kaoru Amano^{1,2)}

5 **Affiliations:**

6 1) Center for Information and Neural Networks (CiNet), National Institute of
7 Information and Communications Technology, and Osaka University, Suita-shi, Osaka,
8 565-0871 Japan

9 2) Graduate School of Frontier Biosciences, Osaka University, Suita-shi, Osaka,
10 565-0871 Japan

11 3) Department of Psychology, New York University, New York, NY, 10003 USA

12 **4. Author contributions:** Designed research: HT KY KA. Performed research: HT.
13 Analyzed data: HT KY. Wrote the paper: HT KY KA.

14 **5. Correspondence should be addressed to:**

15 Hiromasa Takemura

16 Center for Information and Neural Networks (CiNet), National Institute of Information
17 and Communications Technology, and Osaka University
18 1-4 Yamadaoka, Suita-shi, Osaka 565-0871 Japan

19 htakemur@nict.go.jp

20 **6. Number of Figures:** 9

21 **7. Number of Tables:** 0

22 **8. Number of Multimedia:** 0

23 **9. Number of words for Abstract:** 232

24 **10. Number of words for Significance Statement:** 120

25 **11. Number of words for Introduction:** 748

26 **12. Number of words for Discussion:** 2,252

27 **13. Acknowledgments:** We thank Shai Berman for comments on an earlier version of
28 this manuscript and Aviv Mezer for discussions. We thank Hiroshi Ban in support of
29 calibration of visual stimulus presentation environment and Yusuke Sakai in support for
30 data analysis. The funders had no role in study design, data collection and analysis,
31 decision to publish or preparation of the manuscript.

32 **14. Conflict of interest:** Authors report no conflict of interests.

33 **15. Funding sources:** This work was supported by Japan Society for the Promotion of
34 Science (JSPS) KAKENHI (JP17H04684, H.T.; JP16H05862 to K.A.) and Grant-in-Aid
35 for JSPS Fellows (JP15J00412 to H.T., JP16J01822 to K.Y.).

36

37

38 **Abstract:**

39 Although the non-invasive measurement of visually evoked responses has been
40 extensively studied, the structural basis of variabilities in latency in healthy humans is
41 not well understood. We investigated how tissue properties of optic radiation could
42 predict inter-individual variability in the latency of the initial visually evoked component
43 (C1), which may originate from the primary visual cortex. We collected C1 peak latency
44 data using magnetoencephalography (MEG) and checkerboard stimuli, and multiple
45 structural MRI data from 20 healthy subjects. While we varied the contrast and position
46 of the stimuli, the C1 measurement was most reliable when high-contrast stimuli were
47 presented to the lower visual field. We then attempted to predict inter-individual
48 variability in C1 peak latency in this stimulus condition with a multiple regression model
49 using MRI parameters along the optic radiation. We found that this model could predict
50 more than 20% of variance in C1 latency, when the data were averaged across the
51 hemispheres. The model using the corticospinal tract did not predict variability in C1
52 latency, suggesting that there is no evidence for generalization to a non-visual tract. In
53 conclusion, our results suggest that the variability in neural latencies in the early visual
54 cortex in healthy subjects can be partly explained by tissue properties along the optic
55 radiation. We discuss the challenges of predicting neural latency using current structural
56 neuroimaging methods and other factors that may explain inter-individual variance in
57 neural latency.

58

59 **Significance Statement:**

60 Although the non-invasive measurement of visually evoked responses has been studied
61 extensively, the structural basis of variabilities in latency measured in healthy humans is
62 not well understood. We investigated how the tissue properties of the optic radiation
63 could predict inter-individual variability in the latency of the initial visually evoked
64 component (C1). We found that MRI measurements on the optic radiation could partly
65 predict inter-individual variability in C1 latency, while MRI measurements on the
66 corticospinal tract did not. Overall, our work demonstrates that variability of neural
67 latency in the early visual cortex of healthy humans can be partly explained by
68 neuroimaging measurements of tissue properties along the optic radiation, although
69 there are remaining challenges to explain latency variabilities from structural
70 neuroimaging.

71

72 **Introduction**

73 Non-invasive measurement methods, such as electroencephalography (EEG) and
74 magnetoencephalography (MEG), have been widely used to quantify the temporal
75 properties of human cortical responses (Baillet, 2017; Norcia et al., 2015). One of the
76 traditional approaches has been visually evoked responses, which measure the neural
77 response evoked by visual stimuli using EEG or MEG (Adrian and Matthews, 1934;
78 Hämäläinen et al., 1993). This approach has been confirmed to be useful for
79 understanding the neural dynamics underlying visual perception (Amano et al., 2006),
80 attentional modulation of visual processing (Hillyard and Anllo-Vento, 1998), and the
81 development and impairment of the visual system (Braddick et al., 1986; Anderson et al.,
82 1999). Studies using this approach have revealed several major components in human
83 visually evoked responses with a specific range of peak latencies. The variability in
84 these components' latencies provides essential information to understanding the
85 functional properties and disorders of the visual system (Halliday et al., 1972; Thurtell et
86 al., 2009). Measurements of these components evoked by visual stimuli presented to a
87 specific visual field have also been used to assess visual field loss (Kilstorner et al.,
88 1998). Among major components, the earliest is the C1 (also known as N75), which
89 appears in channels located near the occipital pole with a peak latency of 60–100 ms
90 following stimulus onset (Clark et al., 1994; Di Russo et al., 2002). Numerous studies
91 have reported that the cortical source of C1 is the primary visual cortex (V1; Clark et al.,
92 1994; Di Russo et al., 2002; Jeffreys and Axford, 1972). However, while the temporal
93 properties and cortical origins of major visually evoked components have been
94 extensively studied, the question of why healthy humans show large inter-individual
95 differences in peak latency of visually evoked responses, even in the earliest
96 component, remains unanswered.

97 Neurobiological studies suggested that the signal transmission efficiency (conduction
98 velocity) along a long-range axon depends on the microstructural properties of white
99 matter, such as the morphological properties of the myelin sheaths or axons (Cullheim
100 and Ulfhake, 1979; Etxeberria et al., 2016; Pumphrey and Young, 1938; Waxman,
101 1980). We hypothesized that the inter-individual difference in latency of the visually

102 evoked response may be at least partly explained by differences in the tissue in the
103 white matter tracts, which carry signals to visual areas in the cortex.

104 Recent advances in non-invasive structural magnetic resonance imaging (MRI) and
105 tractography have in part enabled us to measure the tissue properties of white matter
106 and the trajectory of the major white matter pathways. Computational modeling of
107 diffusion-weighted MRI (dMRI) signals provides a variety of structural measurements,
108 ranging from those using a simpler diffusion tensor model (Basser and Pierpaoli, 1996)
109 to those using advanced multi-compartment models (Zhang et al., 2012). The recent
110 advent of quantitative T1 (qT1) mapping methods also provides quantitative metrics on
111 white matter tissue properties (Mezer et al., 2013; Weiskopf et al., 2015). However, it is
112 not fully understood how these MRI-based structural measurements along the visual
113 pathway are related to the inter-individual variability of C1 latency in healthy subjects.

114 The visual system is an excellent model system to test a hypothesis concerning
115 microstructural measurements in white matter and functional measurements of neural
116 latencies because both the anatomy of the white matter tract and the major evoked
117 response components are relatively well understood. Moreover, recent advances in
118 tractography algorithms have improved sensitivity for identifying the optic radiation,
119 which carries signals from the lateral geniculate nucleus (LGN) to the V1, from a dMRI
120 dataset (Chamberland et al., 2017; Sherbondy et al., 2008b). The optic radiation has a
121 larger volume and a relatively higher signal-to-noise ratio and is less affected by
122 susceptibility-induced distortions in dMRI measurements than other fiber tracts, i.e., the
123 optic nerve and optic tract. Therefore, we assumed that the optic radiation would be a
124 suitable model pathway to test how MRI-based tissue measurements from the white
125 matter tracts could explain the variability in human V1 response latency, which can be
126 measured as C1 latency using MEG.

127 To this end, we collected visually evoked response data using MEG and structural data
128 for the optic radiation using dMRI and qT1 from 20 healthy subjects. We analyzed how
129 measurements in the optic radiation may predict the inter-individual variability of C1
130 latencies. The goal of this study was to test the extent to which MRI-based tissue
131 measurements along the optic radiation could predict inter-individual variability in C1

132 peak latency in order to understand the extent to which non-invasive structural
133 measurements can explain variability in neural latency in the early visual cortex.

134 **Materials and Methods**

135 **Subjects**

136 Twenty healthy volunteers (15 males, 5 females; age mean \pm standard deviation (SD),
137 28.5 ± 7.96 years-old; ranging from 21-53 years-old) participated in the study. All
138 subjects had a normal or corrected-to-normal vision. dMRI, qT1, and MEG data were
139 collected on different days. The study protocol was approved by the local ethics and
140 safety committees at Center for Information and Neural Networks (CiNet), National
141 Institute of Information and Communications Technology (NICT) and conducted in
142 accordance with the ethical standards stated in the Declaration of Helsinki. Written
143 informed consent was obtained from all study subjects.

144 **MRI experiments**

145 **T1-weighted MRI data acquisition and tissue segmentation**

146 We obtained T1-weighted magnetization-prepared rapid gradient-echo (MP-RAGE)
147 images (1 mm isotropic; repetition time, 1900 ms; echo time, 2.48 ms) from all subjects
148 using a 3T SIEMENS Prisma/Trio scanner at CiNet, NICT to estimate the white/gray
149 matter border. The acquisition of T1-weighted MRI scans took around 15 minutes for
150 each subject. The segmentation was performed using an automated procedure in
151 FreeSurfer software (<https://surfer.nmr.mgh.harvard.edu/>; Fischl, 2012). The tissue
152 segmentation was used for subsequent dMRI and MEG analysis.

153 **Diffusion MRI data acquisition**

154 We measured dMRI data from all subjects. All dMRI data were acquired using the 3T
155 Magnetom Prisma scanner (Siemens, Erlangen, Germany) with a 32-channel head coil
156 at CiNet, NICT. The dMRI data were acquired using monopolar spin-echo planar
157 imaging (EPI; repetition time, 3300 ms; echo time, 66.4 ms; multi-band factor, 3; partial
158 fourier, 5/8; voxel size, $2 \times 2 \times 2 \text{ mm}^3$) implemented in a multi-band accelerated EPI

159 pulse sequence provided by the Center for Magnetic Resonance Research, Department
160 of Radiology, University of Minnesota (Setsompop et al., 2012;
161 <https://www.cmrr.umn.edu/multiband/>). The diffusion weighting was isotropically
162 distributed along 6 directions at $b = 300$ s/mm², 30 directions at $b = 1000$ s/mm², and 64
163 directions at $b = 2000$ s/mm². Eight non-diffusion-weighted ($b = 0$) images were
164 acquired per image set. To minimize EPI distortion, two image sets were acquired with
165 reversed phase-encoding directions (A-P and P-A). The entire dMRI acquisition took
166 around 25 minutes for each subject.

167 **Quantitative T1 data acquisition**

168 We measured qT1 data for all subjects. The qT1 data were acquired using the 3T
169 Magnetom Trio scanner (Siemens, Erlangen, Germany) with a 32-channel head coil at
170 CiNet, NICT and the protocols described in previous publications (Gomez et al., 2017;
171 Mezer et al., 2013). We measured four fast low angle shot (FLASH) images with flip
172 angles of 4°, 10°, 20°, and 30° (repetition time, 12 ms; echo time, 2.41 ms) and an
173 isotropic scan resolution of 1 mm. For the purposes of removing field inhomogeneities,
174 we collected five additional spin echo inversion recovery (SEIR) scans with an EPI
175 readout (repetition time, 3 s; echo time, 49 ms; 2× acceleration). The inversion times
176 were 50, 200, 400, 1200, and 2400 ms. The in-plane resolution and the slice thickness
177 of the additional scan were 2 x 2 mm² and 4 mm, respectively. The entire qT1
178 acquisitions took around 35 min for each subject.

179 **MEG experiment**

180 **MEG data acquisition**

181 In a magnetically shielded room, we measured visually evoked responses from all
182 subjects using a 360-channel whole-head MEG system (Neuromag 360, Elekta) at
183 CiNet, NICT. The MEG system consists of 204 planar gradiometers, 102
184 magnetometers and 54 additional sensors for noise reduction. Magnetic signals were
185 recorded at a sampling frequency of 1,000 Hz. Both planar gradiometers and
186 magnetometers were used for the analysis.

187 **Visual stimuli and task design**

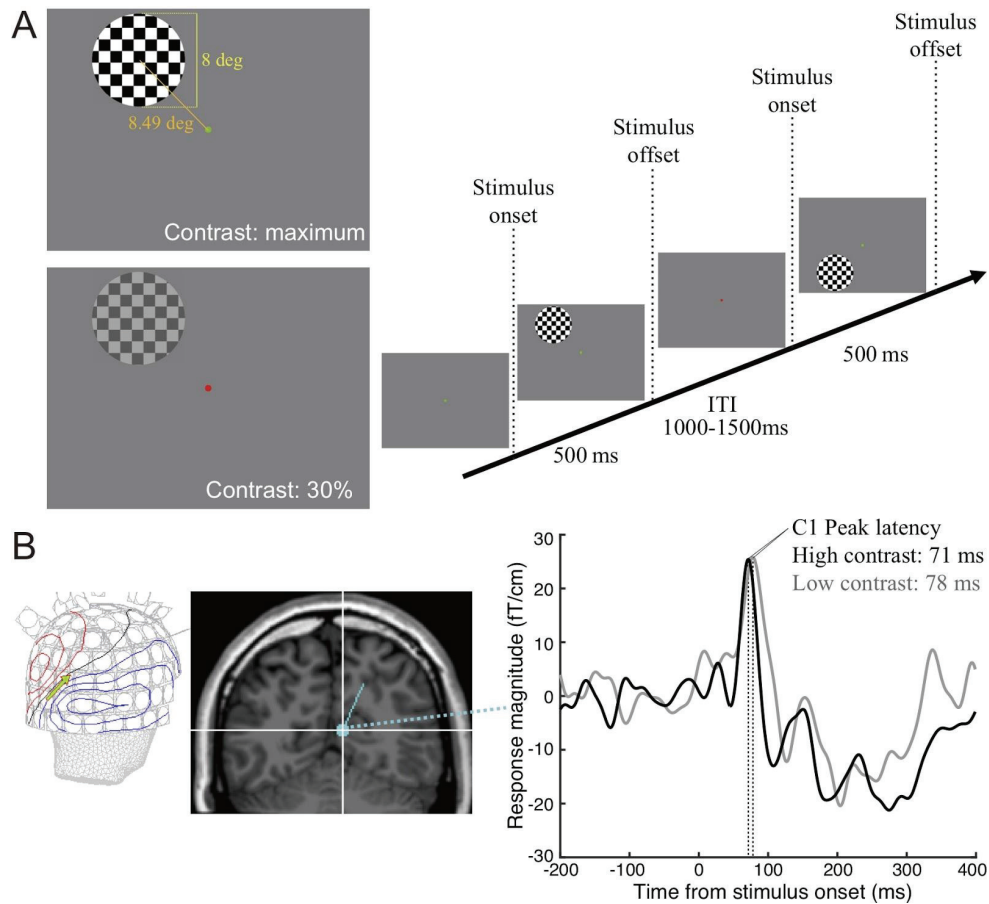
188 Apparatus. Visual stimuli were presented using an LCD projector (PT-DZ680,
189 Panasonic) on a translucent screen in a magnetically shielded room. Gamma correction
190 on the LCD projector was performed using Mcalibrator2 software (Ban and Yamamoto,
191 2013; <https://github.com/hiroshiban/Mcalibrator2>). The projector spanned 27.6×20.7
192 degrees of the visual angle (1024×768 resolution) and had a 60 Hz refresh rate. The
193 viewing distance was 61 cm. Subjects who used glasses wore plastic correction lenses
194 during all MEG measurements. All stimuli were generated using the MATLAB
195 programming environment (MathWorks) and the Psychophysics Toolbox 3 routines
196 (<https://github.com/Psychtoolbox-3/Psychtoolbox-3>; Brainard, 1997).

197 Visual stimuli. The stimuli (Figure 1A) consisted of square-wave circular checkerboards;
198 each stimulus had a diameter of 8 degrees of visual angle and spatial frequency
199 modulation of 0.5 cycles per degree. Eccentricity at the center of the stimuli was 8.49
200 degrees. The stimulus duration was 500 ms. The subjects were asked to maintain
201 fixation on the fixation point (diameter, 0.2 degrees) presented at the center of the
202 screen. Stimulus positions were centered along an arc that was equidistant (8.49
203 degrees) from a central fixation point and located at polar angles of 45° above or below
204 the horizontal meridian (Figure 1A). The stimuli were presented at one of four positions
205 (upper left, lower left, upper right, lower right) and at two different luminance contrast
206 values (30% or maximum Michelson contrast). Visual stimuli were presented binocularly
207 at one of four quadrants and with one of the stimulus contrasts in a randomized
208 sequence. The inter-trial interval was varied between 1,000 and 1,500 ms. Each
209 session consisted of 144 trials (18 trials for each stimulus condition).

210 The total length of each run was approximately 250 seconds. All subjects were tested
211 with twelve such runs, resulting in 216 trials for each stimulus condition. The subjects
212 were able to take a break between runs whenever needed. During the MEG experiment,
213 we logged the stimulus onset of each trial by using a photodiode, which was used to
214 precisely align the MEG signals to the timing of the onset for each stimulus. The entire
215 MEG acquisitions took around 67 minutes for each subject.

216 Task. To maintain an adequate level of alertness and a stable fixation during the
217 experiment, each subject was asked to perform a fixation task. The subject was
218 instructed to press a button when the color of the fixation point (green or red) changed.

219 The change in the fixation color occurs randomly during each run, with no systematic
 220 relationship to stimulus onset or offset. On average, the fixation color changed 61.9
 221 times during each run. The subjects were able to respond to a change in the fixation
 222 color within 1 second on 86.4% of occasions on average.



223

224 **Figure 1. MEG experiment and data analysis.** **A.** Visual stimuli used in the MEG experiment measuring
 225 the visually evoked response. *Left panel:* Example of a checkerboard visual stimulus with high contrast
 226 (upper panel, maximum contrast) and low contrast (lower panel, 30% contrast). *Right panel:* The sequence
 227 of trials. In each trial, the checkerboard stimulus was presented for 500 ms. During the experiment, subjects
 228 were asked to maintain fixation at the red or green dot in the center of the screen and perform a fixation
 229 task. **B. Left panel:** The contour map of magnetic fields in a representative subject (subject 2, lower left
 230 visual field stimulation, high contrast; 71 ms after the stimulus onset). The blue and red contours represent
 231 the sink and source of the magnetic fields, respectively. The green arrow represents the location and

232 direction of the equivalent current dipoles projected on the skull surface. The contour map represents the
233 dipolar field pattern near the occipital pole, suggesting a single source of cortical activity, rather than
234 distributed activity. *Middle panel:* Example of a C1 dipole (left panel) overlaid on a coronal slice of a
235 T1-weighted image (subject 2, left lower visual field stimulation, high contrast). The location of the C1 dipole
236 (blue dot) is near V1 (calcarine sulcus) in the contralateral hemisphere. *Right panel:* The response time
237 course of the C1 dipole (subject 2, lower left visual field stimulation; black curve, high contrast; gray curve,
238 low contrast). In each condition, the C1 peak latency was determined as the time period when the response
239 amplitude of an equivalent current dipole reached the maximum.

240 **Data analyses**

241 **Diffusion MRI data analysis**

242 Preprocessing. dMRI images were corrected for susceptibility-induced distortions using
243 FSL TOPUP tools (Andersson et al., 2003). The eddy current distortions and subject
244 motion in the dMRI images were corrected using FSL EDDY tools (Andersson and
245 Sotiropoulos, 2016).

246 Quantification of tissue measurements. We fitted the diffusion tensor model to the
247 dMRI data using iteratively reweighted linear least squares estimation (Veraart et al.,
248 2013) implemented in MRTrix3 (<http://www.mrtrix.org/>; Tournier et al., 2012). We
249 computed the eigenvalue decomposition of the diffusion tensor imaging (DTI; Basser
250 and Pierpaoli, 1996), and the resulting eigenvalues were used to compute the fractional
251 anisotropy (FA) and mean diffusivity (MD). Furthermore, we fitted a multi-compartment
252 model, neurite orientation dispersion and density imaging (NODDI; Zhang et al., 2012),
253 to the dMRI data using the NODDI MATLAB toolbox
254 (<http://mig.cs.ucl.ac.uk/index.php?n=Tutorial.NODDI matlab>) to obtain intra-cellular
255 volume fraction (ICVF) and orientation dispersion index (ODI) maps.

256 Tractography on the optic radiation. We identified the optic radiation using a dedicated
257 method (ConTrack; Sherbondy et al., 2008a) in view of the known challenges when
258 estimating the human optic radiation using standard whole-brain tractography,
259 particularly tracking of crossing fiber regions around Meyer's loop (Chamberland et al.,
260 2017). First, we estimated the approximate location of the LGN by manual inspection of
261 a T1-weighted image and deterministic tractography from the optic chiasm (Ogawa et

262 al., 2014; Takemura et al., 2019). We then placed an 8-mm radius sphere that covered
263 the LGN endpoints of streamlines from the optic chiasm. Second, we identified the
264 location of the V1 using a probabilistic atlas of retinotopic visual areas (Wang et al.,
265 2015). Using ConTrack, we then sampled 100,000 candidate streamlines connecting
266 LGN and V1 (angle threshold, 90 degrees; step size, 1 mm). Tracking was restricted
267 using the white matter mask generated by tissue segmentation. We selected the top
268 30,000 streamlines with higher scores in the ConTrack scoring process (Sherbondy et
269 al., 2008b). We further excluded streamlines that had either 1) a streamline length of ≥ 5
270 SD longer than the mean streamline length in the tract, or 2) a streamline position of ≥ 5
271 SD away from the mean position of the tract (Yeatman et al., 2012). We identified the
272 optic radiation of each subject separately for two dMRI sessions with reversed phase
273 encoding directions. We then merged the streamlines identified from the two dMRI
274 sessions (Oishi et al., 2018). Further details on the methods used to identify the optic
275 radiation with ConTrack are described in previous papers (Duan et al., 2015; Levin et al.,
276 2010; Malania et al., 2017; Sherbondy et al., 2008b; Takemura et al., 2019).

277 Tractography on the corticospinal tract. The corticospinal tract was used as a control in
278 the analysis since it has no terminations in the occipital cortex, is large in volume, and
279 has a relatively higher signal-to-noise ratio. We used multi-shell multi-tissue constrained
280 spherical deconvolution ($L_{max} = 8$; Jeurissen et al., 2014) to estimate fiber orientation
281 distribution in each voxel using MRTrix3 (Tournier et al., 2012). We performed
282 probabilistic tractography implemented in MRTrix3 to generate 2 million candidate
283 streamlines for each dMRI dataset (step size, 1 mm; maximum angle between
284 successive steps, 45 deg; minimum length, 10 mm; maximum length, 250 mm; fiber
285 orientation distribution amplitude stopping criterion, 0.05). The seed voxels for tracking
286 were randomly chosen from the whole-brain white matter mask. We identified the
287 corticospinal tract from whole-brain streamlines using automated pipelines implemented
288 in the AFQ toolbox (<https://github.com/yeatmanlab/AFQ>; Yeatman et al., 2012)
289 including the outlier streamline exclusion process. Specifically, after identifying the
290 corticospinal tract, we further excluded streamlines that had either 1) a streamline
291 length of ≥ 3 SD longer than the mean streamline length in the tract, or 2) a streamline
292 position of ≥ 3 SD away from the mean position of the tract. We used relatively
293 conservative exclusion criteria for the corticospinal tract since, unlike optic radiation

294 streamlines, streamlines did not pass through another exclusion step (the ConTrack
295 scoring). We identified the corticospinal tract of each subject separately for two dMRI
296 sessions with reversed phase encoding directions. We then merged the streamlines
297 identified from the two dMRI sessions.

298 **Quantitative T1 data analysis**

299 The FLASH and SEIR scans were processed using the mrQ software package
300 (<https://github.com/mezera/mrQ>) in MATLAB to produce the qT1 map. In brief, qT1
301 maps were calculated using variable flip angles which were corrected for B1 excite
302 inhomogeneity using the unbiased SEIR data (Barral et al., 2010). A description of the
303 full analysis pipeline can be found in a previous publication (Mezer et al., 2013).

304 **MEG data analysis**

305 Preprocessing. The recorded MEG signals were first spatiotemporally filtered with the
306 temporal signal space separation (tSSS) method (Taulu et al., 2005; Taulu and Hari,
307 2009) using Maxfilter 2.2.15 (Elekta Neuromag Oy) after removal of the bad channels
308 detected by MEG Xscan tools (Elekta Neuromag Oy). Using Maxfilter, we also roughly
309 transformed the head position in individual subject's data to the head position of a
310 representative subject (subject 1). This process ensures a common channel selection
311 procedure across all subjects in subsequent steps (see below). We further applied
312 bandpass filtering (from 1 to 40 Hz) to MEG signals, which were then averaged across
313 216 trials under each stimulus condition.

314 ECD estimation and identification of C1 peak latency. We used the single equivalent
315 current dipole (ECD) model to estimate the cortical origin of C1 from MEG signals, using
316 the xfit tool (Elekta Neuromag Oy). We chose the single-ECD model because it is an
317 adequate method for the localization of the magnetic field generated by a single
318 localized source, such as in the context of early sensory or motor evoked responses (Di
319 Russo et al., 2002; Salmelin and Hari, 1994; Parkkonen et al., 2009; Maezawa et al.,
320 2016), as compared with methods better suited to distributed cortical responses (e.g.
321 minimum norm estimates methods; Hämäläinen and Ilmoniemi, 1994). We selected 60
322 channels at 20 locations (a magnetometer and two gradiometers at each location) for
323 performing the single ECD analysis. We selected sensors that showed larger visually
324 evoked activation in each stimulus condition based on averaged data for all 20 subjects.

325 After selecting identical pairs of channels across all subjects, an ECD was estimated for
326 single subject data. We performed single dipole fitting to each stimulus condition's data
327 (with regard to stimulus position and contrast) sequentially from 50 ms to 100 ms
328 following stimulus onset. This latency range was chosen for adequate coverage of the
329 onset and peak of C1 reported in a previous study (Di Russo et al., 2002). The dipole
330 fitting was performed with a boundary element method volume conductance model of
331 the individual subject's head based on T1-weighted MRI data. We then selected the
332 ECD with the best goodness-of-fit (GOF) as the representative ECD of C1. In most
333 cases, a single dipolar magnetic field pattern was found in the occipital cortex at around
334 the GOF peak (Figure 1B, left panel), and the ECD was estimated along the calcarine
335 sulcus (Figure 1B, middle panel). We then fixed the dipole position and orientation of
336 the representative ECD over the entire time interval, and estimated the timecourse of
337 the ECD amplitude (Figure 1B, right panel). We identified C1 peak latency as the time
338 period when the ECD amplitude reached maximum (see Figure 1B). C1 peak latency
339 was estimated separately for each stimulus condition (upper or lower visual field; higher
340 or lower contrast). In the main analyses, C1 latency was further averaged across the left
341 and right visual field presentations.

342 Assessment of test-retest reliability. We assessed C1 latency measurement's test-retest
343 reliability by separating MEG data in each stimulus condition into odd and even trials
344 (108 trials for each). We estimated the C1 dipole separately for odd and even trials
345 using a single-ECD model and identified the C1 peak latency. The C1 latencies
346 identified for left and right visual field presentations were averaged. Finally, we
347 evaluated the degree of test-retest reliability by measuring the inter-individual
348 correlation (R) of C1 peak latency between the odd and even trials in four stimulus
349 conditions (upper visual field (UVF)/low contrast, lower visual field (LVF)/low contrast,
350 UVF/high contrast, LVF/high contrast). We estimated the 95% confidence intervals of
351 the correlation coefficient by bootstrap resampling with 10,000 repetitions. Bootstrap
352 analysis was carried out by using the MATLAB Statistics and Machine Learning
353 Toolbox.

354 **Evaluating tissue properties of the optic radiation**

355 We evaluated the tissue properties of the optic radiation based on previously reported
356 methods (Duan et al., 2015; Levin et al., 2010; Minami et al., 2020; Takemura et al.,
357 2019; Yeatman et al., 2012). Briefly, we resampled each streamline to 100 equidistant
358 nodes. The tissue properties were calculated at each node of each streamline using
359 spline interpolation of the tissue properties quantified by a diffusion tensor model (FA
360 and MD), NODDI (ICVF and ODI) and qT1. The qT1 maps were registered with the
361 dMRI data for each subject and the qT1 values along each node of each streamline
362 were computed. The properties at each node were summarized by taking a weighted
363 average of tissue property measurement (FA, MD, qT1, ICVF, and ODI) on each
364 streamline within that node. The weight of each streamline was based on the
365 Mahalanobis distance from the tract core, which is calculated as the mean of each
366 streamline's x, y, z coordinates at each node (Yeatman et al., 2012). We excluded the
367 first and last 10 nodes from the tissue property of the tract core to exclude voxels close
368 to the gray/white matter interface where the tract is likely to be heavily intersected with
369 other fibers, such as those in the superficial U-fiber system. We then averaged 80
370 values at different nodes along the optic radiation for each MRI parameter to obtain
371 subject-specific tissue properties. The measurement from the dMRI data (FA, MD, ICVF
372 and ODI) was averaged across two runs. Finally, we averaged each MRI parameter
373 across the left and right hemispheres.

374 **Predicting C1 latency from tissue properties of white** 375 **matter**

376 Full model. We fitted the linear multiple regression models in which C1 peak latency
377 was predicted by the linear weighted sum of five MRI parameters (FA, MD, qT1, ICVF
378 and ODI) along the optic radiation with a constant (c):

$$379 \text{ C1 latency} = w_{\text{FA}} * \text{FA} + w_{\text{MD}} * \text{MD} + w_{\text{qT1}} * \text{qT1} + w_{\text{ICVF}} * \text{ICVF} + w_{\text{ODI}} * \text{ODI} + c \quad (1)$$

380 Model fitting was performed using the MATLAB Statistics and Machine Learning
381 Toolbox with the objective of minimizing the least squared error by selecting the best
382 combination of weights and constant.

383 Reduced models. We evaluated the performance of three different reduced models,
384 which used a subset of MRI parameters.

385 *DTI + NODDI model:*

$$386 \quad C1 \text{ latency} = w_{FA} * FA + w_{MD} * MD + w_{ICVF} * ICVF + w_{ODI} * ODI + c \quad (2)$$

387 *DTI + qT1 model:*

$$388 \quad C1 \text{ latency} = w_{FA} * FA + w_{MD} * MD + w_{qT1} * qT1 + c \quad (3)$$

389 *NODDI + qT1 model:*

$$390 \quad C1 \text{ latency} = w_{qT1} * qT1 + w_{ICVF} * ICVF + w_{ODI} * ODI + c \quad (4)$$

391 Full + tract length model. We also estimated a tract length of the optic radiation in each
 392 subject by calculating the mean length of the streamlines belonging to the optic
 393 radiation. The tract lengths in the left and right optic radiation were averaged. We then
 394 tested a model incorporating the estimated tract length into the full model for predicting
 395 C1 peak latency.

$$396 \quad C1 \text{ latency} = w_{FA} * FA + w_{MD} * MD + w_{qT1} * qT1 + w_{ICVF} * ICVF + w_{ODI} * ODI \\ 397 \quad \quad \quad + w_{length} * length + c \quad (5)$$

398 Full + V1 cortical thickness (CT) model. We finally estimated the cortical thickness
 399 (CT) of the V1 (defined by probabilistic retinotopy atlas; Wang et al., 2015) based on the
 400 FreeSurfer segmentation (see above). Next, we tested a model that incorporated the V1
 401 CT into the full model for predicting C1 peak latency.

$$402 \quad C1 \text{ latency} = w_{FA} * FA + w_{MD} * MD + w_{qT1} * qT1 + w_{ICVF} * ICVF + w_{ODI} * ODI + w_{CT} * CT + c \quad (6)$$

403 **Evaluation of model performance**

404 Leave-one-out cross-validation was used to evaluate how well the models predicted C1
 405 peak latency. Specifically, we divided the data from all subjects into 19 training datasets
 406 and 1 test dataset to evaluate how much each model could predict C1 latency in a
 407 subject that was not included in the model fitting phase. We iterated this procedure 20
 408 times by changing the selection of the test dataset. We evaluated the accuracy of the
 409 model by calculating a Pearson correlation coefficient (cross-validated R) across the
 410 measured C1 latency and the C1 latency predicted from a linear multiple regression
 411 model.

412 We also evaluated the statistical significance of the model prediction using a
413 permutation test. We randomly shuffled the association between MRI measurements
414 and C1 peak latency across all subjects 10,000 times. After each shuffle, we performed
415 a model prediction from MRI measurements to C1 peak latency using a multiple linear
416 regression model and leave-one-out cross-validation to obtain a correlation coefficient
417 (R). We then calculated the percentile of the original correlation coefficient with respect
418 to the distribution of the correlations calculated over the 10,000 permutations. This
419 percentile is reported as the P -value, which is the likelihood of randomly acquiring the
420 original correlation value.

421 For the Full model, in order to estimate the contribution of each MRI parameter, we also
422 performed a linear multiple regression analysis on data from 20 subjects without
423 performing a leave-one-out cross validation. We reported the t -value and P -value for
424 each MRI parameter on the linear multiple regression of the Full model in order to
425 quantify the likelihood of the contribution of each MRI parameter with regard to latency
426 prediction.

427 **Software Accessibility**

428 The code for reproducing figures and statistical analyses in this work will be publicly
429 available online via a public repository
430 (<https://github.com/htakemur/PredictingLatencyfromOR>) upon the acceptance of the
431 manuscript. The code was written in MATLAB and tested in MATLAB 2015a on Ubuntu
432 14.04 LTS.

433 **Results**

434 We sought to test the extent to which the inter-individual difference in C1 latency
435 depends on the MRI-based tissue properties measurements of the optic radiation. While
436 several studies have previously demonstrated the test-retest reliability of dMRI and qT1
437 measurements (Vollmar et al., 2010; Mezer et al., 2013; Chung et al., 2016), such
438 analyses are rarely carried out on MEG measurements. Therefore, we first evaluated
439 the variability and test-retest reliability of the MEG measurements on C1 latency across
440 the different stimulus conditions. We then tested the extent to which MRI measurements

441 of the optic radiation could predict inter-individual variability in C1 latency under the
442 stimulus condition with the highest reproducibility. We also evaluated the accuracy of
443 C1 prediction from a non-visual white matter tract (the corticospinal tract). Finally, we
444 assessed how much tissue measurements along the optic radiation could predict C1
445 latency in response to visual stimuli presented in the contralateral visual field.

446 **Distribution, stimulus dependence and test-retest** 447 **reliability of C1 peak latency**

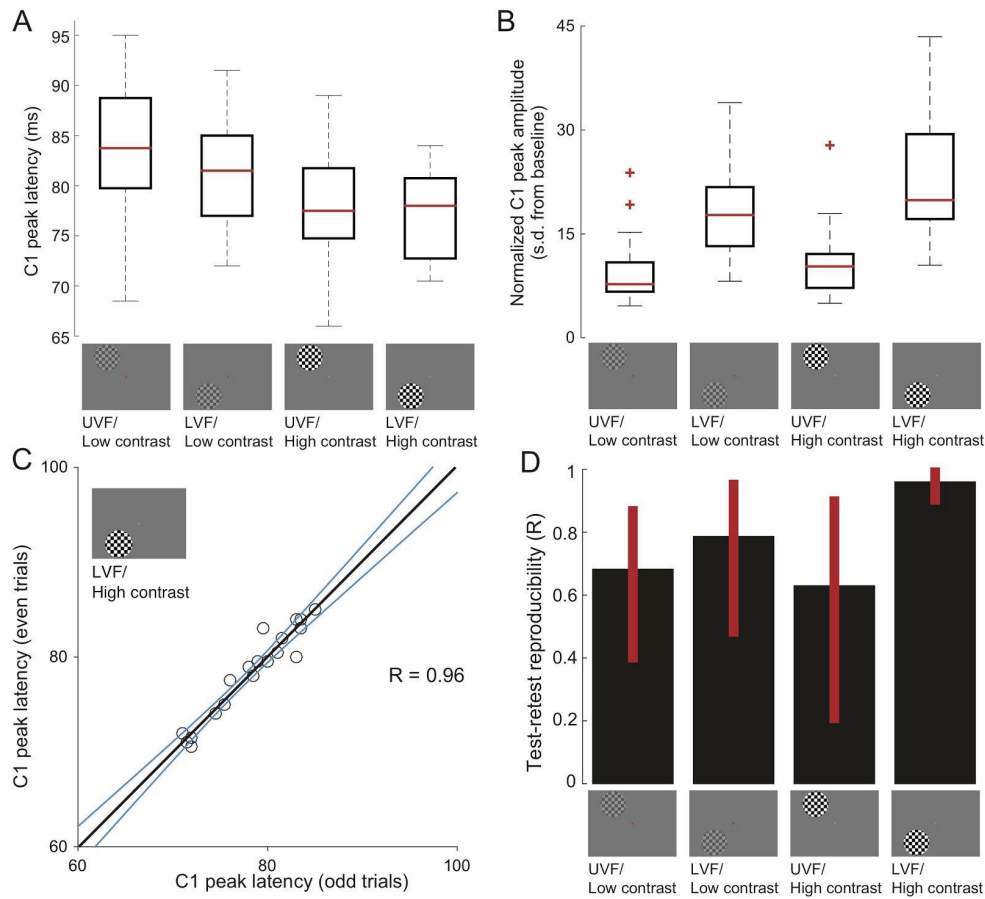
448 First, we evaluated the extent to which the properties of C1 depend on the stimulus
449 conditions used in our MEG experiment (upper or lower visual field; low or high contrast;
450 the data in the left and right visual field stimulus presentation were averaged). Figure 2A
451 shows a box plot of C1 peak latency in each stimulus condition. Under all conditions, the
452 C1 peak latency ranged from 65 to 95 milliseconds after the stimulus onset. The range
453 of C1 peak latency was consistent with the range reported in a previous study that used
454 similar checkerboard stimuli (Di Russo et al., 2002). The mean C1 peak latencies
455 across subjects were 83.6, 81.0, 77.8, and 77.4 milliseconds for each stimulus condition
456 (UVF/low contrast, LVF/low contrast, UVF/high contrast and LVF/high contrast,
457 respectively). We also found notable inter-individual differences in C1 peak latency (with
458 standard deviations of 7.4, 5.2, 6.2 and 4.3 ms for each stimulus condition). There was
459 no significant correlation between C1 peak latency and subject age under all stimulus
460 conditions ($R = 0.11, 0.12, -0.13, \text{ and } 0.04$; $P = 0.65, 0.62, 0.57 \text{ and } 0.88$, for each
461 stimulus condition).

462 To evaluate how much C1 latency depends on the stimulus condition, we performed
463 two-way analysis of variance on the C1 peak latency data (with contrast and stimulus
464 position as main effects). We found that the main effect of contrast was significant ($F_{1,76}$
465 $= 12.59, P = 0.0007$), while the main effect of visual field (upper or lower) and the
466 interaction between contrast and visual field were not (main effect of visual field, $F_{1,76} =$
467 $1.30, P = 0.26$; interaction between contrast and visual field; $F_{1,76} = 0.70, P = 0.41$),
468 suggesting that C1 latency was significantly delayed in the lower contrast condition.

469 We also evaluated the amplitude of the response at C1 peak latency (Figure 2B), which
470 was normalized using the mean and SD of the amplitude during the baseline period
471 (-200 to -1 ms from the stimulus onset). We found that the main effect of visual field was

472 significant ($F_{1,76} = 48.17$, $P < 0.0001$) while the main effect of contrast was only
473 marginally significant ($F_{1,76} = 3.37$, $P = 0.07$). The interaction between visual field and
474 contrast was not statistically significant ($F_{1,76} = 0.77$, $P = 0.38$). This result suggests that
475 the amplitude of the C1 response was significantly larger for the stimuli presented at the
476 LVF in contrast to those presented at the UVF. A larger C1 response for LVF stimuli is
477 consistent with previous reports (Fortune and Hood, 2003; Hagler et al., 2009;
478 Maruyama et al., 2009; Portin et al., 1999; Tzelepi et al., 2001). In summary, we
479 identified C1 peak latency within the range reported in a previous study (Di Russo et al.,
480 2002), and found that its latency and magnitude significantly depended on the stimulus
481 contrast and position.

482 Next, we sought to identify the stimulus condition providing the most reliable C1 peak
483 latency by assessing the test-retest reliability. To this end, we separately estimated the
484 C1 dipole in odd and even trials (108 trials for each) and identified the C1 peak latency
485 in each condition. We observed the highest reproducibility of C1 latency when high
486 contrast stimuli were presented at the LVF (Figure 2C; $R = 0.96$) as compared with low
487 contrast stimuli presented at the LVF ($R = 0.79$) or low/high contrast stimuli presented at
488 the UVF ($R = 0.68$ and 0.63 for low and high contrast, respectively; Figure 2D). The
489 higher reproducibility in the LVF conditions may be related to the higher signal-to-noise
490 ratio under these conditions. Considering that the reproducibility of C1 peak latency in
491 the high contrast, LVF condition far exceeded that of the other conditions, we primarily
492 used the C1 latency data in this stimulus condition for subsequent analyses using MRI
493 data.



494

495 **Figure 2. Properties of the C1 peak latency/amplitude measured by MEG.** **A.** Distribution of C1 peak
 496 latency in four stimulus conditions (UVF, Upper Visual Field; LVF, Lower Visual Field). Mean C1 latencies in
 497 each condition are depicted as red lines. The border of the black box indicates the 25% and 75%
 498 percentiles in each condition. The error bars with a dotted line indicate the range of C1 latency for all
 499 subjects. **B.** Distribution of the C1 peak amplitude in four different stimulus conditions. The vertical axis
 500 depicts the extent to which C1 peak amplitude was deviated from mean response amplitude during the
 501 baseline period (-200 to -1 ms from the stimulus onset) with a unit of standard deviation of the response
 502 amplitude within the baseline period. The red cross indicates outlier data (outside ± 2.7 standard deviations
 503 within a distribution in each condition). Other conventions are identical to those in Figure 2A. **C.** A scatter
 504 plot comparing C1 peak latency in odd trials (horizontal axis) and even trials (vertical axis) when high
 505 contrast stimuli were presented at the LVF. Each individual dot depicts the C1 peak latency in each
 506 individual subject and the black line is a linear regression line. The blue curves indicate the 95% confidence
 507 interval of a linear regression estimated by the bootstrapping method. **D.** Test-retest reliability under all

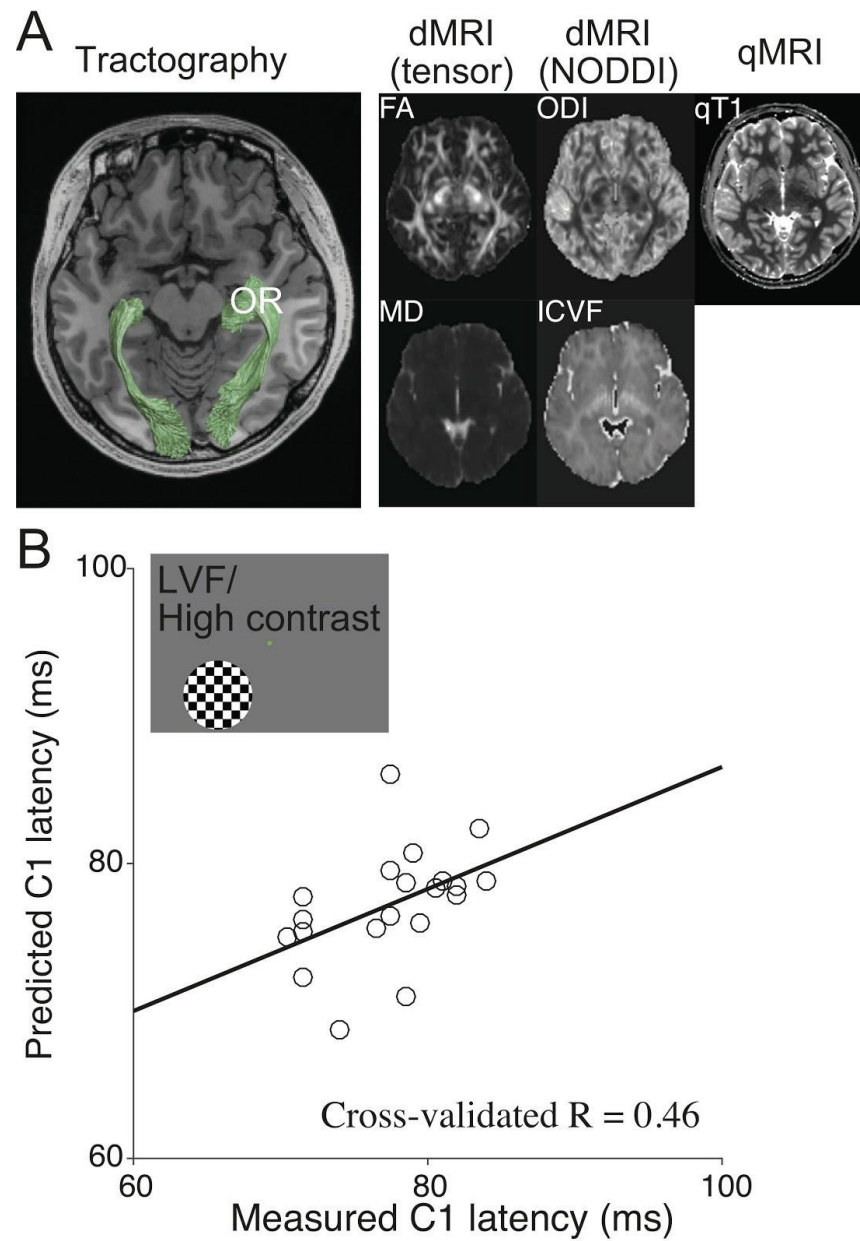
508 stimulus conditions. The vertical axis depicts the correlation coefficient (R) of C1 peak latency between the
509 odd and even trials. The error bar depicts the 95% confidence interval of the correlation coefficient
510 estimated by the bootstrapping method (see Materials and Methods).

511 **Predicting C1 latency from tissue properties of the optic** 512 **radiation**

513 Using the dMRI data, we identified the optic radiation in all 20 subjects using
514 probabilistic tractography). Figure 3A (left panel) represents the optic radiation identified
515 from dMRI data in a representative subject. From the dMRI data, we estimated four
516 tissue property measurements by using the diffusion tensor model (FA and MD) and the
517 multi-compartment model (ODI and ICVF). We also measured $qT1$ by using an MRI
518 acquisition protocol distinct from dMRI (see Materials and Methods). We then estimated
519 five MRI parameters (FA, MD, ODI, ICVF and $qT1$; Figure 3A, right panel) along the
520 optic radiation. We used these five MRI parameters, since previous works
521 demonstrated that these parameters may be sensitive to different types of
522 microstructural properties of brain tissues (Mezer et al., 2013; Crombe et al., 2018). We
523 then used a linear multiple regression model to predict the inter-individual variability of
524 C1 peak latency from the five MRI-based tissue measurements along the optic radiation.
525 We evaluated the performance of the model by leave-one-out cross-validation to test
526 the ability of the model to predict C1 latency of the test dataset that was not used to train
527 the model.

528 Figure 3B depicts the comparison between the measured and predicted C1 latencies for
529 the high contrast stimuli presented to the LVF, which is a condition with a highest
530 test-retest reliability (Figure 2D). The model explained 22% of the variance ($R^2 = 0.22$)
531 in inter-individual variability of C1 latency ($R = 0.46$; Figure 3B). Next, we estimated the
532 statistical significance of the model performance using a permutation test and found that
533 its performance was statistically significant ($P = 0.01$). The result for this most reliable
534 condition suggests that the inter-individual variability of C1 peak latency can be at least
535 partly explained by variability in tissue properties along the optic radiation. The
536 prediction accuracy for other stimulus conditions was variable (Figure 4; $R = 0.70, 0.21$
537 and 0.53 ; $P = 0.0002, 0.20$ and 0.008 for UVF/low contrast, LVF/low contrast, UVF/high
538 contrast, respectively). As discussed above, given the large difference in the

539 reproducibility of C1 peak latency across the stimulus conditions (Figure 2D), we
 540 focused on the LVF/high contrast condition in subsequent analyses.

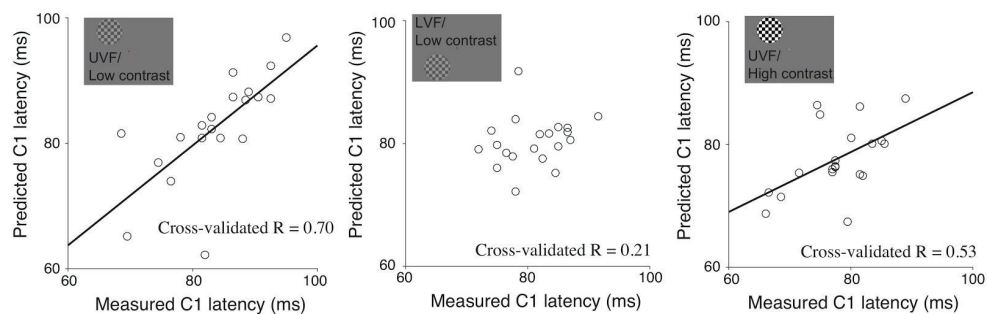


541

542 **Figure 3. Prediction of the C1 peak latency from the tissue properties of the optic radiation.** *A. Left*
 543 *panel:* The optic radiation (OR, green) in a representative subject (subject 9) identified using tractography in

544 the dMRI dataset overlaid on an axial slice of a T1-weighted image. *Right panel:* MRI-based tissue property
 545 maps in the same subject. **B.** Comparison between the measured C1 peak latency (horizontal axis) and the
 546 C1 peak latency predicted from the optic radiation (vertical axis) when a higher contrast stimulus was
 547 presented at the lower visual field (LVF). The model prediction was performed by dividing 20 subjects into
 548 19 training datasets and one test dataset (leave-one-out cross-validation) and iterating 20 times by
 549 changing the test subject. Each datapoint indicates the measured and predicted C1 latency for an individual
 550 subject. The model showed a significant performance to predict C1 peak latency (cross-validated $R = 0.46$;
 551 $P = 0.01$). The black line depicts the linear regression between the measured and predicted C1 latency.

552



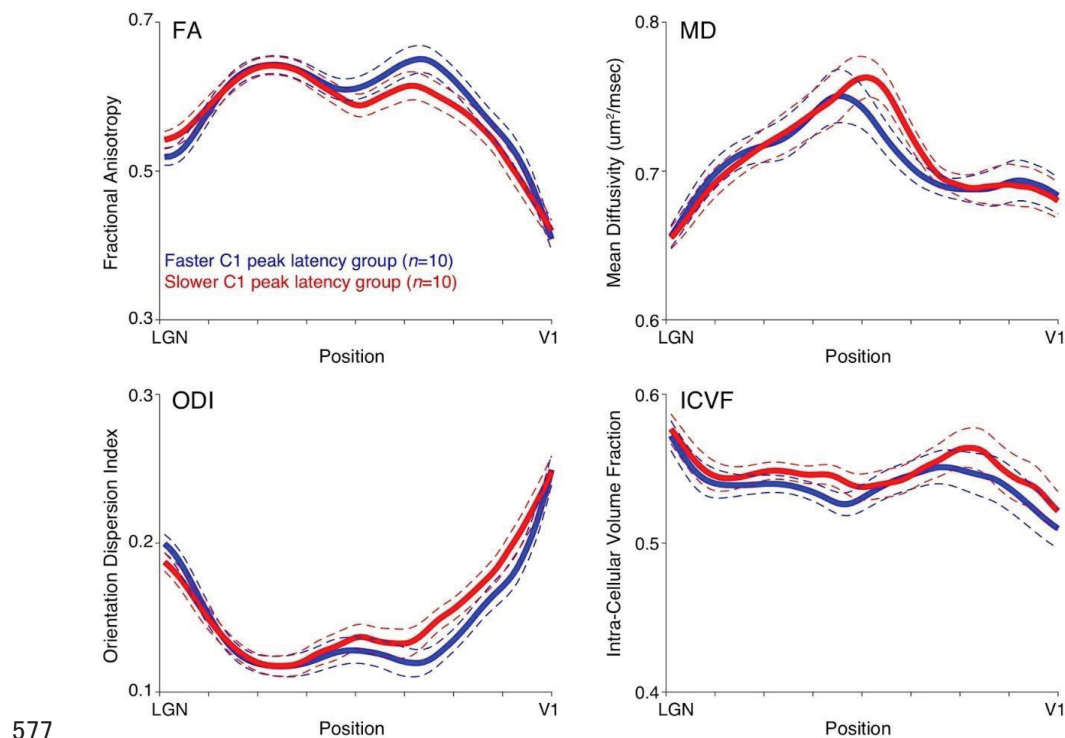
553

554 **Figure 4. Prediction accuracy of the C1 latency in the other three stimulus conditions.** *Left panel:*
 555 *UVF/low contrast, Middle panel: LVF/low contrast, Right panel: UVF/high contrast.* These three conditions
 556 have a relatively lower test-retest reproducibility of C1 measurement (see Figure 2D). Conventions are
 557 identical to those in Figure 3B.

558 In the main analysis, we used five MRI parameters to predict the variabilities in C1
 559 latency. We sought to identify MRI parameters that contributed to predicting C1 latency
 560 in the LVF/high contrast condition. To this end, we calculated t-values for each MRI
 561 measurement along the optic radiation in a linear multiple regression model predicting
 562 C1 peak latency. Here we used the data from all 20 subjects and found that all MRI
 563 parameters except for qT1 significantly contributed to the prediction of C1 peak latency
 564 in the high contrast condition ($t = 2.46, 2.82, -0.77, 2.70, \text{ and } -2.41, P = 0.03, 0.01, 0.45,$
 565 $0.02, \text{ and } 0.03$ for FA, MD, qT1, ODI, and ICVF, respectively).

566 To understand which part of the optic radiation contributed to the prediction of the C1
 567 peak latency, we also calculated how much the spatial profile of MRI parameters
 568 depended upon C1 peak latency. Figure 5 represents the spatial profile of four

569 parameters (FA, MD, ODI and ICVF) along the optic radiation contributing to C1 peak latency
 570 latency prediction in subjects with faster ($n=10$) and slower ($n=10$) C1 peak latencies.
 571 Group differences in each parameter were not significant ($t_{18} = 1.00, -0.19, -0.96$ and
 572 -0.60 ; $P = 0.33, 0.85, 0.35$ and 0.56 for FA, MD, ODI and ICVF), suggesting that
 573 individual parameters may not be sufficient for C1 peak latency prediction. Meanwhile,
 574 small group differences were found mostly in the middle to posterior part of the optic
 575 radiation (closer to V1), suggesting that voxels along the straight portion of the optic
 576 radiation may contribute to C1 peak latency prediction.

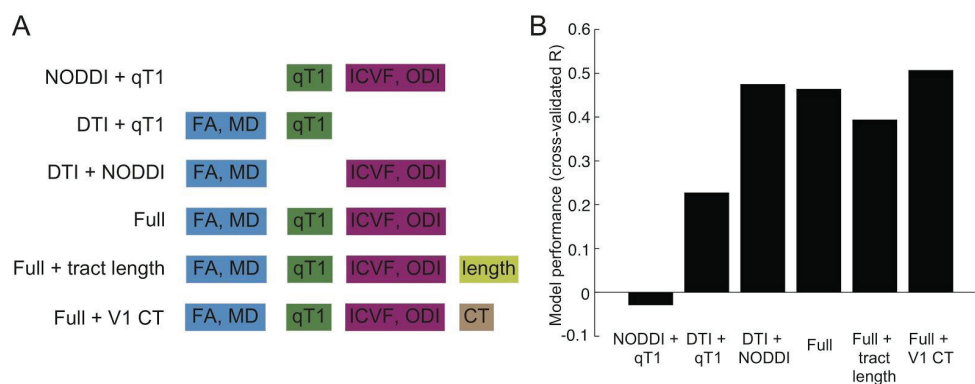


577

578 **Figure 5. Tissue properties along the optic radiation.** The four panels show the FA (left upper panel),
 579 MD (right upper panel), ODI (left lower panel) and ICVF (right lower panel) measurements, respectively.
 580 The mean profiles of subjects with faster (blue, $n = 10$) and slower C1 peak latencies (red, $n = 10$) are
 581 represented as thick solid curves. The thin dotted curves represent values ± 1 s.e.m. from the group mean.
 582 The horizontal axis represents the normalized position along the optic radiation (left: anterior, right:
 583 posterior).

584 In the main analysis, we used five MRI parameters to measure tissue properties of the
 585 optic radiation. These parameters were estimated by different diffusion modelling
 586 methods (DTI or NODDI) or different scanning sequences (dMRI or qT1). We further
 587 tested how much variance in C1 peak latency under the LVF/high contrast condition
 588 could be predicted by a subset of MRI parameters. We compared the performance of
 589 the full model using all five parameters with that of three reduced models using a subset
 590 of parameters (Figure 6A). The performance of the model without qT1 (DTI-NODDI
 591 model; $R = 0.46$; Figure 6B) was comparable with that of the full model ($R = 0.46$). The
 592 full model outperformed the other models using a subset of parameters (DTI-qT1 model,
 593 $R = 0.23$; NODDI-qT1 model, $R = -0.03$; Figure 6B). These results suggest that different
 594 diffusivity parameters (FA, MD, ODI, and ICVF) may contribute to predicting C1 peak
 595 latency in a complementary way, while qT1 did not contribute.

596 Finally, we compared the performance of the model when including either the mean
 597 optic radiation streamline length or the cortical thickness (CT) of the V1 as an
 598 explanatory variable in addition to the MRI parameters (Full + tract length model, Full +
 599 V1 CT model; Figure 6A). The model incorporating streamline length had modest
 600 performance for predicting C1 peak latency ($R = 0.39$), but did not outperform the full
 601 model used in the main analysis (Figure 6B). The model incorporating the CT of the V1
 602 slightly outperformed the full model ($R = 0.51$). Therefore, we did not find evidence that
 603 information on streamline length improves the prediction accuracy for C1 peak latency
 604 although there remains a possibility that some structural properties of the gray matter
 605 (V1) may provide further information relevant to predicting C1 latency.



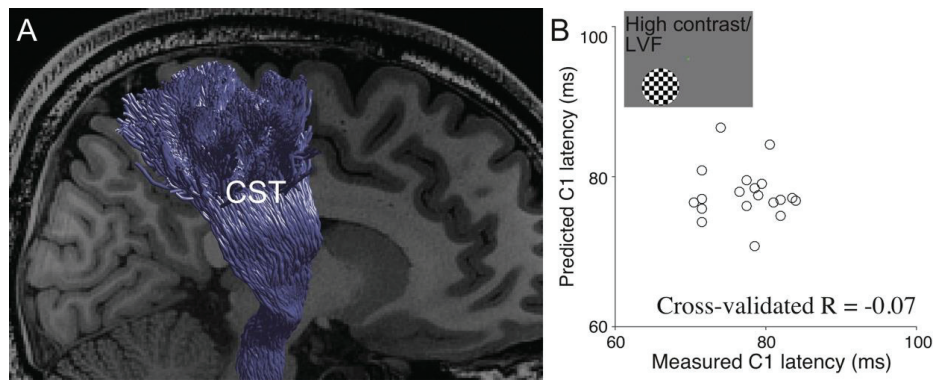
606

607 **Figure 6. Comparison of prediction accuracy for C1 peak latency in a lower visual field/high**
608 **contrast condition between the models. A.** Schematic of the model. We compared the model tested in
609 the main analysis (“Full model”), with six variants. We tested three types of reduced models that use a
610 subset of MRI parameters along the optic radiation. We also tested a model including the streamline length
611 of the optic radiation or cortical thickness (CT) of the V1 as an explanatory variable (“Full + tract length”
612 model; “Full + V1 CT” model). **B.** Model performance. The vertical axis shows the correlation coefficient (R)
613 between the measured and predicted C1 latency in each model, which was estimated by leave-one-out
614 cross validation.

615 **Tissue properties along the corticospinal tract did not** 616 **predict variability in C1 latency**

617 We then evaluated how well the model using a non-visual tract (corticospinal tract;
618 Figure 7A) could predict C1 peak latency in order to clarify the extent to which prediction
619 accuracy observed in the optic radiation is generalizable to other white matter tracts.
620 We used an identical number of MRI parameters (FA, MD, qT1, ODI, and ICVF) to
621 predict C1 peak latency in a representative condition (LVF/high contrast) and evaluated
622 the accuracy of the model using the identical leave-one-out cross-validation procedure.

623 The corticospinal tract model did not significantly predict inter-individual variability of C1
624 peak latency in the high contrast/low visual field condition ($R = -0.07$; $P = 0.60$; Figure
625 7B). We also confirmed that this model did not significantly predict C1 peak latency
626 under any other stimulus conditions ($R = -0.11, 0.02, \text{ and } -0.34$; $P = 0.67, 0.47, \text{ and } 0.92$
627 for UVF/low contrast, LVF/low contrast, UVF/high contrast). These results suggest that
628 the prediction accuracy observed in the optic radiation cannot be generalized to a
629 non-visual white matter tract.



630

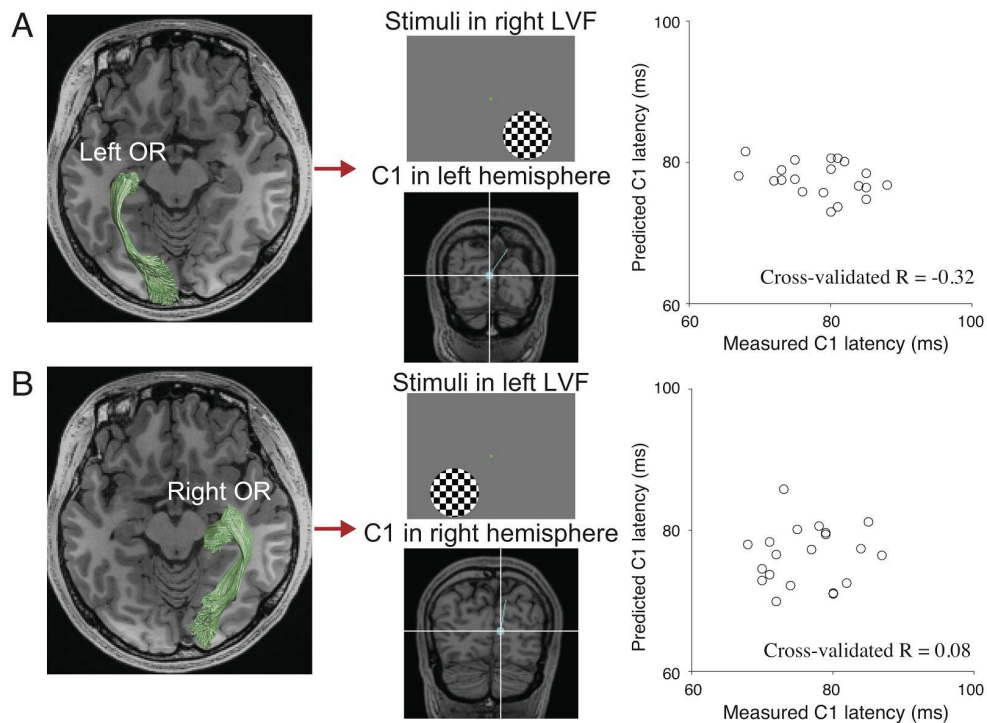
631 **Figure 7. Prediction of C1 peak latency from the corticospinal tract (CST).** **A.** The CST in a
 632 representative subject (subject 9) identified using tractography in the dMRI dataset overlaid on a sagittal
 633 slice of a T1-weighted image. **B.** Comparisons between the measured C1 peak latencies (horizontal axis)
 634 and the C1 peak latencies predicted from the CST (vertical axis) when a higher contrast stimulus was
 635 presented at the LVF. The model did not reveal a significantly successful performance in predicting C1
 636 peak latency (cross-validated $R = -0.07$; $P = 0.60$).

637 **Do tissue properties of the optic radiation predict C1** 638 **latency to stimuli presented in the contralateral visual** 639 **field?**

640 The human V1 responds predominantly to visual stimuli in the contralateral visual field.
 641 The cortical source of C1 also appears in the hemisphere contralateral to the visual field
 642 position of the presented stimuli (Di Russo et al., 2002). Therefore, we hypothesized
 643 that if we subdivided the optic radiation data into the left and right hemispheres, the
 644 tissue measurements along the optic radiation may predict the C1 peak latency to visual
 645 stimuli presented in the contralateral visual field.

646 As a result, the C1 peak latency evoked by the right and left LVF stimuli (high contrast)
 647 cannot be predicted by the properties of the optic radiation in the contralateral
 648 hemisphere (C1 latency in the right LVF, $R = -0.32$, $P = 0.92$, Figure 8A; C1 latency in
 649 the left LVF, $R = 0.08$, $P = 0.36$, Figure 8B). A lack of hemispheric specificity poses a
 650 challenge when interpreting the significant prediction accuracy for averaged data and
 651 suggests that there are still challenges remaining in terms of robust prediction of the

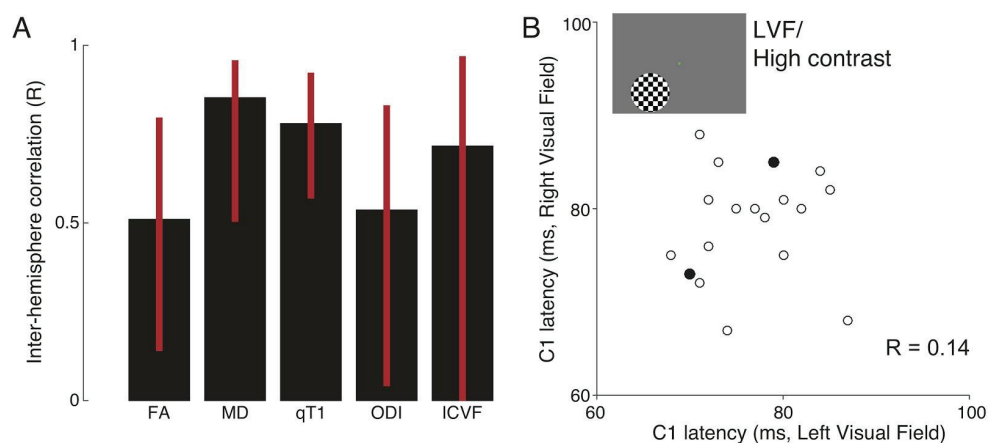
652 neural response latency from MRI-based tissue property measurements in white matter
 653 pathways.



654
 655 **Figure 8. The optic radiation tissue properties from a single hemisphere did not predict C1 latency**
 656 **in response to high contrast stimuli presented in the contralateral lower visual field. A.** Prediction of
 657 C1 peak latency evoked by high contrast stimuli in the right LVF from the left optic radiation (left panel). The
 658 dipole at a time around the C1 peak latency was localized to the calcarine sulcus in the left hemisphere
 659 (middle panel, subject 9). The prediction accuracy did not reach a statistically significant level ($R = -0.32$; P
 660 $= 0.92$). **B.** Prediction of C1 peak latency evoked by high contrast stimuli in the left LVF from the right optic
 661 radiation (left panel). The dipole at a time around the C1 peak latency was localized to the calcarine sulcus
 662 in the right hemisphere (middle panel). The prediction accuracy did not reach a statistically significant level
 663 ($R = 0.08$; $P = 0.36$) in this case as well.

664 To clarify the reason for which there was such a large difference in prediction accuracy
 665 between the averaged and single hemisphere data, we assessed the inter-hemispheric
 666 correlation of MRI measurements and C1 peak latency (Figure 9). The MRI
 667 measurements along the optic radiation correlated across the hemispheres, while a
 668 degree of correlation varies across metrics ($R = 0.51, 0.85, 0.78, 0.54,$ and 0.72 for FA,

669 MD, qT1, ODI, and ICVF, respectively; Figure 9A). In contrast, the C1 peak latency
 670 under the LVF/high contrast condition did not correlate between stimulation to the left
 671 and right visual field ($R = 0.14$, Figure 9B). We noted that the test-retest reliability of the
 672 C1 peak latency in each visual field was considerably high (right LVF/high contrast, $R =$
 673 0.91 ; left LVF/high contrast, $R = 0.94$) such that the hemispheric differences in C1 peak
 674 latency are reproducible, rather than a product of unstable MEG measurements. These
 675 findings suggest that the lack of hemispheric specificity might be due to the fact that
 676 MRI measurements are correlated across hemispheres while MEG measurements are
 677 not. This may be a simple consequence of the fact that MRI measurements have
 678 insufficient sensitivity to be able to identify inter-hemispheric latency differences, since
 679 some estimates of MRI measurements in a single hemisphere may be noisy given a
 680 relatively lower inter-hemisphere correlations in FA and ODI or a larger confidence
 681 interval of inter-hemisphere correlation in ICVF (Figure 9A). Alternatively, it is also
 682 plausible that an anatomical or physiological factor other than the tissue properties of
 683 the optic radiation may be eliciting a hemispheric difference in C1 latency.



684
 685 **Figure 9.** Correlation of measurements across hemispheres and visual fields. **A.** Correlation coefficient (R)
 686 of MRI measurements along the optic radiation across the left and right hemispheres. The error bar depicts
 687 the 95% confidence interval estimated by the bootstrapping method. **B.** There is no significant correlation
 688 for C1 latency between the left and right visual field condition (LVF/high contrast stimulus). The open circles
 689 indicate data points from a single subject, and the filled circle shows the datapoints that overlapped
 690 between two subjects.

691

692 **Discussion**

693 The aim of this study was to determine the ability of MRI-based tissue measurements
694 along the human optic radiation to predict inter-individual variability in C1 peak latency,
695 which is the earliest component of visually evoked responses. Analysis of the optic
696 radiation data averaged across the hemispheres predicted 22% of variance in C1 peak
697 latency for high-contrast stimuli presented in the LVF, for which we obtained the highest
698 test-retest reproducibility of C1 peak latency. Analysis of the corticospinal tract revealed
699 that the prediction accuracy observed in the optic radiation may not be generalizable to
700 non-visual white matter tracts. The optic radiation measurements along the left/right
701 hemisphere failed to predict C1 peak latency to visual stimuli presented in the
702 contralateral visual field. In summary, we found evidence that inter-individual variability
703 in C1 peak latency can be explained in part by the tissue properties of the optic radiation
704 under specific stimulus conditions. Below, we discuss the relationship between this
705 study and previous literature and current limitations in neuroimaging approach.

706 **What factors may better explain inter-individual** 707 **variability in C1 peak latency?**

708 In this study, we found evidence to suggest that the tissue properties of the optic
709 radiation in part explain inter-individual variability in C1 latency. However, there are
710 several other factors that may be relevant for C1 peak latency.

711 *Latency difference in the retina.* Another factor that could account for the inter-individual
712 variability in C1 peak latency is inter-individual variability in response latency in retinal
713 cells. In humans, this has been widely assessed using the electroretinogram (ERG;
714 McCulloch et al., 2015). However, inter-individual variability of ERG peak latency is
715 reported to be very small in healthy subjects (e.g., the standard deviation in healthy
716 subjects was 1–2 ms in a previous study; Gauvin et al., 2014). Therefore, it is unlikely
717 that variability in latency of retinal cells would explain a large part of variance in
718 inter-individual variability of C1 peak latency, which is on the order of 10–20 ms (Figures
719 2A and 4B).

720 Pupil size and retinal illumination. Previous studies demonstrated a significant
721 relationship between pupil size and latency of visually evoked responses by artificially
722 varying the pupil size of human subjects (Hawkes and Stow, 1981; Martins et al., 2003).
723 Another line of study demonstrated that latency of visually evoked response was
724 delayed by decreasing retinal illumination (Froehlich and Kaufman, 1991). Given
725 that previous studies demonstrated inter-individual difference in pupil size (Higuchi et
726 al., 2008; Aminihajbashi et al., 2019), since we did not control for retinal illumination, we
727 cannot exclude the possibility that the variability in these factors during the MEG
728 experiment may have affected the measurements of C1 peak latencies. Therefore,
729 incorporating these factors may improve the precision of the C1 latency prediction from
730 MRI measurements on the optic radiation.

731 Optic nerve and optic tract. In this study, we could not incorporate the tissue properties
732 of the earlier visual white matter tract, i.e., the optic nerve and optic tract, into the model
733 used to predict variance in C1 peak latency because of the greater difficulties involved
734 in obtaining reliable measurements from these tracts as compared with the optic
735 radiation. The optic nerve is particularly difficult to measure using standard dMRI
736 acquisitions because it is prone to susceptibility-induced distortions and signal dropout.
737 The optic tract is also prone to measurement difficulties because of a relatively small
738 signal-to-noise ratio and small volume, which may cause partial volume effects with
739 cerebrospinal fluid. It may be challenging to perform this type of analysis using a
740 higher-order model like NODDI to assess tissue properties in the optic tract. Advanced
741 measurement methods, such as readout-segmented EPI, hold promise in terms of
742 improving the quality of dMRI measurements in these tracts (Frost et al., 2015; Kida et
743 al., 2016; Porter and Heidemann, 2009) and providing more information to predict C1
744 peak latency in future investigations.

745 Tract length. Variability in the tract length could also explain the inter-individual
746 difference in C1 peak latency. To explore this hypothesis, we included tract length
747 (mean length across all optic radiation streamlines in each subject) as an explanatory
748 variable in the model but did not find any improvement in prediction accuracy (see
749 Results section). A potential limitation of this approach is that streamlines only
750 approximate the trajectory of fiber bundles and are not true axons, so may not fully
751 capture inter-individual variability in length of the optic radiation fibers. Indeed, fibers in

752 the optic radiation may change their position along the tract (Nelson and LeVay, 1985),
753 and it is not fully clear whether or not streamline lengths are useful for approximation of
754 fiber length. Better understanding of the significance of fiber length may require
755 additional assessment using anatomical methods and advanced modelling.

756 *Difference in latency derived from processing of neural information in gray matter.* Peak
757 latency measured using MEG or EEG may reflect build-up process of local field
758 potential but does not directly reflect the response latency of spiking activity in
759 single-neuron electrophysiology. Such a response profile may involve multiple
760 physiological factors, such as information integration or the degree of synchrony
761 between neurons in the gray matter (Hermes et al., 2017). In fact, incorporating the
762 cortical thickness of V1 into the model provided a modest improvement in the accuracy
763 of the latency prediction, although the neurobiological interpretation of MRI-based
764 estimates on cortical thickness remains an area of active investigation (la Fougère et al.,
765 2011; Wagstyl et al., 2020). An improved understanding of the relationship between
766 anatomy and physiology is required to understand what type of anatomical features are
767 useful for characterizing inter-individual latency variability derived from neural
768 information processing in the gray matter.

769 *Cortical feedback.* A number of anatomical, electrophysiological and neuroimaging
770 studies have demonstrated the existence of feedback signal from the extrastriate cortex
771 to the V1 (Rockland and Virga, 1986; Lamme et al., 1998; Girard et al., 2001; Muckli et
772 al., 2015; Rockland, 2020). A study on non-human primates revealed that feedback
773 signals from extrastriate cortex affect visually-evoked responses of V1 neurons at a
774 very early phase (i.e. 10 ms after response onset; Hupé et al., 2001). Therefore, it is
775 likely that not only feedforward but also feedback signals from extrastriate areas affect
776 the C1, limiting the accuracy of the C1 peak latency prediction solely based on the
777 structural properties of the optic radiation.

778 **Related studies**

779 Previous studies have demonstrated delayed visually evoked responses in patients with
780 demyelinating diseases, such as multiple sclerosis (Halliday et al., 1972; Thurtell et al.,
781 2009). More recent studies have demonstrated a correlation between diffusivity
782 measurements along the early visual white matter pathway and the latency of visually

783 evoked responses in multiple sclerosis patients (Alshowaier et al., 2014; Takemura et
784 al., 2017). Price and colleagues (2017) also demonstrated that an age-related delay in
785 the visually evoked response can be predicted from diffusivity measurement on the
786 optic radiation. These studies suggest that MRI-based white matter measurements
787 could provide useful information for prediction of variability in visually evoked responses,
788 if such inter-individual variability in latency was disease-related or age-dependent. The
789 present results suggest that such predictive power may be at least partly generalizable
790 to relatively small inter-individual differences between healthy subjects.

791 Horowitz and colleagues (2015a) tested the relationship between dMRI-based
792 measurements (AxCaliber or FA) of white matter properties and conduction velocities
793 measured by EEG. Although the interpretation of their findings has remained
794 controversial (Horowitz et al., 2015b; Innocenti et al., 2015), these authors successfully
795 demonstrated a correlation between white matter measurements and latency
796 measurements in healthy subjects (Horowitz et al., 2015a). One notable difference from
797 our study is that they investigated a correlation between white matter measurements in
798 the corpus callosum and interhemispheric delay of visual or tactile evoked responses
799 measured by EEG. Since the corpus callosum has a relatively uniform fiber orientation
800 within voxels, and a large number of histological measurements have been performed,
801 it may be relatively easy to make an inference about the underlying microstructure from
802 MRI-based measurements (Alexander et al., 2010; Barazany et al., 2009; Berman et al.,
803 2019, 2018; Huang et al., 2015; Stikov et al., 2015). In contrast, fibers in the optic
804 radiation change their orientation and position within a tract before reaching the terminal
805 (Nelson and LeVay, 1985) and also cross with other neighboring pathways
806 (Chamberland et al., 2017). We speculate that the lack of hemisphere-specific
807 correlation in this study may be partly due to the fact that identifying the microstructural
808 properties using MRI measurements in the optic radiation is more difficult than in the
809 corpus callosum.

810 **Current challenges in neuroimaging measurements**

811 This study did not provide evidence of generalization across all different stimulus
812 conditions (Figure 4) and of hemispheric specificity (Figure 8). These results may reflect
813 some limitations in this study. One notable limitation is the relatively smaller sample size

814 ($N = 20$) used to elucidate inter-individual variability, which may have limited the
815 statistical power of the study. However, in addition to a limitation in statistical power,
816 there are several existing challenges to current neuroimaging measurements for
817 establishing associations between structural measurements in white matter pathways
818 and measurements of neural response latency in humans.

819 In addition to the issues related to the signal qualities in the optic nerve and optic tract,
820 as discussed above, dMRI measurements have limited spatial and angular resolution.
821 Improved measurement methods may improve our ability to assess the properties of
822 tissue in the visual white matter pathways without influence of a partial volume effect
823 with other neighboring pathways or cerebrospinal fluid. Furthermore, improved dMRI
824 data acquisition method may improve the accuracy of tractography on the optic
825 radiation (Chamberland et al., 2018). There are ongoing efforts to improve the signal
826 quality and resolution of dMRI (Roebroek et al., 2019; Setsompop et al., 2018), and to
827 develop post-processing methods on improving dMRI data resolution (Alexander et al.,
828 2017).

829 dMRI-based tractography is an excellent approach to identifying trajectories of major
830 white matter pathways like the optic radiation (Rokem et al., 2017). However, in terms of
831 current knowledge, it is not fully clear how much variance in MRI measurements along
832 optic radiation voxels can be explained by properties of feedforward pathways from the
833 LGN to V1, because there may be other pathways that partly pass through the same
834 white matter regions. Anatomical studies in non-human primates have reported the
835 existence of feedback connections from V1 to the LGN (Angelucci and Sainsbury, 2006;
836 Ichida and Casagrande, 2002). Although Heinrich Sachs, a classical neuroanatomist,
837 proposed that feedforward and feedback pathways may pass through a different white
838 matter region (Sachs, 1892), the spatial organization of these pathways along the optic
839 radiation in humans is not well understood. Moreover, other studies reported the
840 existence and importance of pathways connecting the pulvinar and visual cortex
841 (Baldwin et al., 2017; Bridge et al., 2016; Kaas and Lyon, 2007). It may be that the
842 pulvino-cortical pathways in humans pass partly through the common voxel as LGN-V1
843 pathways at the resolution of dMRI. It is likely that contamination between the
844 feedforward LGN-V1 pathway and other pathways within the same voxel poses a
845 challenge for predicting V1 latency from a structural MRI dataset.

846 MEG measurements also pose challenges in terms of comparison with dMRI and qT1
847 data. For example, if we could obtain reliable peak latency measurements from the LGN,
848 we could calculate the conduction velocity from the LGN to V1 for comparison with the
849 tissue properties of the optic radiation. While recent studies have reported that the early
850 peak of a visually evoked response can be localized to the LGN, it is difficult to obtain
851 such a response in a consistent manner across all subjects (Yoshida et al., 2017). We
852 also note that, while most studies have reported that C1 primarily originates from V1, we
853 could not fully exclude the influence of signals from neighboring areas (such as V2 and
854 V3), due to the limitations inherent to the precise estimation of source localizations.

855 We may also need to improve biophysical models to better understand the relationship
856 between MRI measurements and underlying white matter microstructure. While
857 microstructural modelling of MRI data for the corpus callosum has been successful
858 (Assaf et al., 2008; Berman et al., 2019, 2018; Horowitz et al., 2015a; Stikov et al.,
859 2015), generalization from the corpus callosum to the optic radiation may require
860 additional work and validation. Another recent study also found that axonal conduction
861 velocity depends not only on the myelin g-ratio (the ratio between the inner and outer
862 diameters of the myelin sheath) but also on myelin internode length highlighting a need
863 to include additional microstructural information to further understand the conduction
864 velocity (Etxeberria et al., 2016).

865 Finally, although peak latency is fairly reproducible and widely mentioned in the
866 literature, the extent to which peak latency could represent the neuronal response
867 latency in the visual system is debatable. For example, a limitation of peak latency is
868 that it does not distinguish between a signal that starts early and rises slowly and a
869 signal that starts late and rises rapidly (Norcia et al., 2015). Modeling of the relationship
870 between the MEG signal and the underlying neuronal response properties will be
871 essential to reduce the limitations of MEG measurements of neuronal latency in future
872 investigations.

873 In conclusion, we found that individual differences in latency of the early visually evoked
874 response in humans can be partly explained by the differences in tissue along the optic
875 radiation. Although the model using tissue properties of the optic radiation explained
876 approximately 20% of variance in C1 peak latency, other factors may need to be

877 incorporated into the model to improve our understanding of the structural-functional
878 relationship in the early visually evoked response in humans.

879 **References**

- 880 Adrian ED, Matthews BH (1934) The interpretation of potential waves in the cortex. *J.*
881 *Physiol.* 81:440–471.
- 882 Alexander DC, Hubbard PL, Hall MG, Moore EA, Ptito M, Parker GJM, Dyrby TB
883 (2010) Orientationally invariant indices of axon diameter and density from diffusion
884 MRI. *NeuroImage* 52:1374–1389.
- 885 Alexander DC, Zikic D, Ghosh A, Tanno R, Wotschel V, Zhang J, Kaden E, Dyrby TB,
886 Sotiropoulos SN, Zhang H, Criminisi A (2017) Image quality transfer and
887 applications in diffusion MRI. *NeuroImage* 152:283–298.
- 888 Alshowaier D, Yiannikas C, Garrick R, Parratt J, Barnett MH, Graham SL, Klistorner A
889 (2014) Latency of multifocal visual evoked potentials in nonoptic neuritis eyes of
890 multiple sclerosis patients associated with optic radiation lesions. *Invest.*
891 *Ophthalmol. Vis. Sci.* 55:3758–3764.
- 892 Amano K, Goda N, Nishida S, Ejima Y, Takeda T, Ohtani Y (2006) Estimation of the
893 timing of human visual perception from magnetoencephalography. *J.*
894 *Neurosci.* 26:3981–3991.
- 895 Aminihajbashi S, Hagen T, Foldal MD, Laeng B, Espeseth T (2019) Individual
896 differences in resting-state pupil size: evidence for association between working
897 memory capacity and pupil size variability. *Int J Psychophysiol.* 140:1–7.
- 898 Anderson SJ, Holliday IE, Harding GF (1999) Assessment of cortical dysfunction in
899 human strabismic amblyopia using magnetoencephalography (MEG). *Vision Res.*
900 39:1723–1738.
- 901 Andersson JLR, Skare S, Ashburner J (2003) How to correct susceptibility distortions
902 in spin-echo echo-planar images: application to diffusion tensor imaging.
903 *NeuroImage* 20:870–888.
- 904 Andersson JLR, Sotiropoulos SN (2016) An integrated approach to correction for
905 off-resonance effects and subject movement in diffusion MR imaging. *NeuroImage*
906 125:1063–1078.

- 907 Angelucci A, Sainsbury K (2006) Contribution of feedforward thalamic afferents and
908 corticogeniculate feedback to the spatial summation area of macaque V1 and LGN.
909 *J. Comp. Neurol.* 498:330–351.
- 910 Assaf Y, Blumenfeld-Katzir T, Yovel Y, Basser PJ (2008) Axc caliber: A method for
911 measuring axon diameter distribution from diffusion MRI. *Magn. Reson. Med.*
912 59:1347–1354.
- 913 Baillet S (2017) Magnetoencephalography for brain electrophysiology and imaging. *Nat.*
914 *Neurosci.* 20:327–339.
- 915 Baldwin MKL, Balaram P, Kaas JH (2017) The evolution and functions of nuclei of the
916 visual pulvinar in primates. *J. Comp. Neurol.* 525:3207–3226.
- 917 Ban H, Yamamoto H (2013) A non–device-specific approach to display
918 characterization based on linear, nonlinear, and hybrid search algorithms. *J. Vis.*
919 13, 6:20.
- 920 Barazany D, Basser PJ, Assaf Y (2009) In vivo measurement of axon diameter
921 distribution in the corpus callosum of rat brain. *Brain* 132:1210–1220.
- 922 Barral JK, Gudmundson E, Stikov N, Etezadi-Amoli M, Stoica P, Nishimura DG (2010)
923 A robust methodology for in vivo T1 mapping. *Magn. Reson. Med.* 64:1057–1067.
- 924 Basser PJ, Pierpaoli C (1996) Microstructural and physiological features of tissues
925 elucidated by quantitative-diffusion-tensor MRI. *J. Magn. Reson. B* 111:209–219.
- 926 Berman S, West KL, Does MD, Yeatman JD, Mezer AA (2018) Evaluating g-ratio
927 weighted changes in the corpus callosum as a function of age and sex.
928 *NeuroImage* 182:304–313.
- 929 Berman S, Filo S, Mezer AA (2019) Modeling conduction delays in the corpus callosum
930 using MRI-measured g-ratio. *NeuroImage* 195:128–139.
- 931 Braddick OJ, Wattam-Bell J, Atkinson J (1986) Orientation-specific cortical responses
932 develop in early infancy. *Nature* 320:617–619.
- 933 Brainard DH (1997) The psychophysics toolbox. *Spat. Vis.* 10:433–436.
- 934 Bridge H, Leopold DA, Bourne JA (2016) Adaptive pulvinar circuitry supports visual
935 cognition. *Trends Cogn. Sci.* 20:146–157.
- 936 Chamberland M, Scherrer B, Prabhu SP, Madsen J, Fortin D, Whittingstall K,
937 Descoteaux M, Warfield SK (2017) Active delineation of Meyer’s loop using
938 oriented priors through MAGNETic tractography (MAGNET). *Hum. Brain Mapp.*
939 38:509–527.

- 940 Chamberland M, Tax CMW, Jones DK (2018) Meyer's loop tractography for
941 image-guided surgery depends on imaging protocol and hardware. *NeuroImage*
942 *Clin* 20:458–465.
- 943 Chung AW, Seunarine KK, Clark CA (2016) NODDI reproducibility and variability with
944 magnetic field strength: A comparison between 1.5 T and 3 T. *Human Brain Mapp*
945 37:4550–4565.
- 946 Clark VP, Fan S, Hillyard SA (1994) Identification of early visual evoked potential
947 generators by retinotopic and topographic analyses. *Hum. Brain Mapp.* 2:170–
948 187.
- 949 Crombe A, Planche V, Raffard G, Bourel J, Dubourdieu N, Panatier A, Fukutomi H,
950 Dousset V, Oilet S, Hiba B, Tourdias T (2018) Deciphering the microstructure of
951 hippocampal subfields with in vivo DTI and NODDI: applications to experimental
952 multiple sclerosis. *NeuroImage* 172:357–368.
- 953 Cullheim S, Ulfhake B (1979) Relations between cell body size, axon diameter and
954 axon conduction velocity of triceps surae alpha motoneurons during the postnatal
955 development in the cat. *J. Comp. Neurol.* 188:679–686.
- 956 Di Russo F, Martínez A, Sereno MI, Pitzalis S, Hillyard SA (2002) Cortical sources of
957 the early components of the visual evoked potential. *Hum. Brain Mapp.* 15:95–
958 111.
- 959 Duan Y, Norcia AM, Yeatman JD, Mezer A (2015) The structural properties of major
960 white matter tracts in strabismic amblyopia. *Invest. Ophthalmol. Vis. Sci.* 56:5152–
961 5160.
- 962 Etxeberria A, Hokanson KC, Dao DQ, Mayoral SR, Mei F, Redmond SA, Ullian EM,
963 Chan JR (2016) Dynamic modulation of myelination in response to visual stimuli
964 alters optic nerve conduction velocity. *J. Neurosci.* 36:6937–6948.
- 965 Fischl B (2012) FreeSurfer. *NeuroImage* 62:774–781.
- 966 Fortune B, Hood DC (2003) Conventional pattern-reversal VEPs are not equivalent to
967 summed multifocal VEPs. *Invest. Ophthalmol. Vis. Sci.* 44:1364–1375.
- 968 Froehlich J, Kaufman DI (1991) Effect of decreased retinal illumination on
969 simultaneously recorded pattern electroretinograms and visual-evoked potentials.
970 *Invest. Ophthalmol. Vis. Sci.* 32:310–318.

- 971 Frost R, Jezzard P, Douaud G, Clare S, Porter DA, Miller KL (2015) Scan time
972 reduction for readout-segmented EPI using simultaneous multislice acceleration:
973 Diffusion-weighted imaging at 3 and 7 Tesla. *Magn. Reson. Med.* 74:136–149.
- 974 Gauvin M, Lina J-M, Lachapelle P (2014) Advance in ERG analysis: from peak time
975 and amplitude to frequency, power, and energy. *Biomed Res. Int.* 2014:246096.
- 976 Girard P, Hupé JM, Bullier J (2001) Feedforward and feedback connections between
977 areas V1 and V2 of the monkey have similar rapid conduction velocities. *J*
978 *Neurophysiol* 85:1328–1331.
- 979 Gomez J, Barnett MA, Natu V, Mezer A, Palomero-Gallagher N, Weiner KS, Amunts K,
980 Zilles K, Grill-Spector K (2017) Microstructural proliferation in human cortex is
981 coupled with the development of face processing. *Science* 355:68–71.
- 982 Hagler DJ Jr, Halgren E, Martinez A, Huang M, Hillyard SA, Dale AM (2009) Source
983 estimates for MEG/EEG visual evoked responses constrained by multiple,
984 retinotopically-mapped stimulus locations. *Hum. Brain Mapp.* 30:1290–1309.
- 985 Halliday AM, McDonald WI, Mushin J (1972) Delayed visual evoked response in optic
986 neuritis. *Lancet* 1:982–985.
- 987 Hämäläinen M, Hari R, Ilmoniemi RJ, Knuutila J, Lounasmaa OV (1993)
988 Magnetoencephalography---theory, instrumentation, and applications to
989 noninvasive studies of the working human brain. *Rev. Mod. Phys.* 65:413–497.
- 990 Hämäläinen MS, Ilmoniemi RJ (1994) Interpreting magnetic fields of the brain:
991 minimum norm estimates. *Med Biol Eng Comput.* 32:35–42.
- 992 Hawkes CH, Stow B (1981) Pupil size and the pattern evoked visual response. *J*
993 *Neurol Neurosurg Psychiatry.* 44:90–91.
- 994 Hermes D, Nguyen M, Winawer J (2017) Neuronal synchrony and the relation between
995 the blood-oxygen-level dependent response and the local field potential. *PLoS Biol.*
996 15:e2001461.
- 997 Higuchi S, Ishibashi K, Aritake S, Enomoto M, Hida A, Tamura M, Kozaki T, Motohashi
998 Y, Mishima K (2008) Inter-individual difference in pupil size correlates to
999 suppression of melatonin by exposure to light. *Neurosci Lett.* 440:23–26.
- 1000 Hillyard SA, Anllo-Vento L (1998) Event-related brain potentials in the study of visual
1001 selective attention. *Proc. Natl. Acad. Sci. U. S. A.* 95:781–787.

- 1002 Horowitz A, Barazany D, Tavor I, Bernstein M, Yovel G, Assaf Y (2015a) In vivo
1003 correlation between axon diameter and conduction velocity in the human brain.
1004 *Brain Struct. Funct.* 220:1777–1788.
- 1005 Horowitz A, Barazany D, Tavor I, Yovel G, Assaf Y (2015b) Response to the comments
1006 on the paper by Horowitz et al. (2014). *Brain Struct. Funct.* 220:1791–1792.
- 1007 Huang SY, Nummenmaa A, Witzel T, Duval T, Cohen-Adad J, Wald LL, McNab JA
1008 (2015) The impact of gradient strength on in vivo diffusion MRI estimates of axon
1009 diameter. *NeuroImage* 106:464–472.
- 1010 Hupé JM, James AC, Girard P, Lomber SG, Payne BR, Bullier J (2001) Feedback
1011 connections act on the early part of the responses in monkey visual cortex. *J*
1012 *Neurophysiol.* 85:134–145.
- 1013 Ichida JM, Casagrande A (2002) Organization of the feedback pathway from striate
1014 cortex (V1) to the lateral geniculate nucleus (LGN) in the owl monkey (*Aotus*
1015 *trivirgatus*). *J. Comp. Neurol.* 454:272–283.
- 1016 Innocenti GM, Caminiti R, Aboitiz F (2015) Comments on the paper by Horowitz et al.
1017 (2014). *Brain Struct. Funct.* 220:1789–1790.
- 1018 Jeffreys DA, Axford JG (1972) Source locations of pattern-specific components of
1019 human visual evoked potentials. I. Component of striate cortical origin. *Exp. Brain*
1020 *Res.* 16:1–21.
- 1021 Jeurissen B, Tournier J-D, Dhollander T, Connelly A, Sijbers J (2014) Multi-tissue
1022 constrained spherical deconvolution for improved analysis of multi-shell diffusion
1023 MRI data. *NeuroImage* 103:411–426.
- 1024 Kaas JH, Lyon DC (2007) Pulvinar contributions to the dorsal and ventral streams of
1025 visual processing in primates. *Brain Res Rev* 55:285–296.
- 1026 Klistorner AI, Graham SL, Grigg JR, Billson FA (1998) Multifocal topographic visual
1027 evoked potential: improving objective detection of local visual field defects. *Invest.*
1028 *Ophthalmol. Vis. Sci.* 39:937–950.
- 1029 Kida I, Ueguchi T, Matsuoka Y, Zhou K, Stemmer A, Porter D (2016) Comparison of
1030 diffusion-weighted imaging in the human brain using readout-segmented EPI and
1031 PROPELLER turbo spin echo with single-shot EPI at 7 T MRI. *Invest. Radiol.* 51:
1032 435–439.
- 1033 la Fougère C, Grant S, Kostikov A, Schirmacher R, Gravel P, Schipper HM, Reader A,
1034 Evans A, Thiel A (2011) Where in-vivo imaging meets cytoarchitectonics: the

- 1035 relationship between cortical thickness and neuronal density measured with
1036 high-resolution [18F] flumazenil-PET. *NeuroImage* 56:951–960.
- 1037 Lamme VA, Super H, Spekreijse H (1998) Feedforward, horizontal, and feedback
1038 processing in the visual cortex. *Current Opin Neurobiol.* 8:529–535.
- 1039 Levin N, Dumoulin SO, Winawer J, Dougherty RF, Wandell BA (2010) Cortical maps
1040 and white matter tracts following long period of visual deprivation and retinal image
1041 restoration. *Neuron* 65:21–31.
- 1042 Maezawa H, Mima T, Yazawa S, Matsushashi M, Shiraishi H, Funahashi M (2016)
1043 Cortico-muscular synchronization by proprioceptive afferents from the tongue
1044 muscles during isometric tongue protrusion. *NeuroImage* 128:284–292.
- 1045 Malania M, Konrad J, Jäggle H, Werner JS, Greenlee MW (2017) Compromised integrity
1046 of central visual pathways in patients with macular degeneration. *Invest.*
1047 *Ophthalmol. Vis. Sci.* 58:2939–2947.
- 1048 Martins A, Balachandran C, Klistorner AI, Graham SL, Billson FA (2003) Effect of pupil
1049 size on multifocal pattern visual evoked potentials. *Clin Exp Ophthalmol.* 31:354–356.
- 1050 Maruyama M, Palomo DD, Ioannides AA (2009) Stimulus-contrast-induced biases in
1051 activation order reveal interaction between V1/V2 and human MT+. *Hum. Brain*
1052 *Mapp.* 30:147–162.
- 1053 McCulloch DL, Marmor MF, Brigell MG, Hamilton R, Holder GE, Tzekov R, Bach M
1054 (2015) ISCEV Standard for full-field clinical electroretinography (2015 update).
1055 *Doc. Ophthalmol.* 130:1–12.
- 1056 Mezer A, Yeatman JD, Stikov N, Kay KN, Cho NJ, Dougherty RF, Perry ML, Parvizi J,
1057 Hua le H, Butts-Pauly K, Wandell BA (2013) Quantifying the local tissue volume
1058 and composition in individual brains with magnetic resonance imaging. *Nat. Med.*
1059 19:1667–1672.
- 1060 Minami S, Oishi H, Takemura H, Amano K (2020) Inter-individual differences in
1061 occipital alpha oscillations correlate with white matter tissue properties of the optic
1062 radiation. *eNeuro.* 7:ENEURO.0224-19.2020.
- 1063 Muckli L, De Martino F, Vizioli L, Petro LS, Smith FW, Ugurbil K, Goebel R, Yacoub E
1064 (2015) Contextual feedback to superficial layers of V1. *Curr Biol.* 25:2690–2695.
- 1065 Nelson SB, LeVay S (1985) Topographic organization of the optic radiation of the cat. *J.*
1066 *Comp. Neurol.* 240:322–330.

- 1067 Norcia AM, Appelbaum LG, Ales JM, Cottareau BR, Rossion B (2015) The
1068 steady-state visual evoked potential in vision research: A review. *J. Vis.* 15, 6:4.
- 1069 Ogawa S, Takemura H, Horiguchi H, Terao M, Haji T, Pestilli F, Yeatman JD, Tsuneoka
1070 H, Wandell BA, Masuda Y (2014) White matter consequences of retinal receptor
1071 and ganglion cell damage. *Invest. Ophthalmol. Vis. Sci.* 55:6976–6986.
- 1072 Oishi H, Takemura H, Aoki SC, Fujita I, Amano K (2018) Microstructural properties of
1073 the vertical occipital fasciculus explain the variability in human stereoacuity. *Proc.*
1074 *Natl. Acad. Sci. U. S. A.* 115:12289-12294.
- 1075 Parkkonen L, Fujiki N, Mäkelä JP (2009) Sources of auditory brainstem responses
1076 revisited: contribution by magnetoencephalography. *Human Brain Mapp.*
1077 30:1772–1782.
- 1078 Porter DA, Heidemann RM (2009) High resolution diffusion-weighted imaging using
1079 readout-segmented echo-planar imaging, parallel imaging and a two-dimensional
1080 navigator-based reacquisition. *Magn Res Med.* 62:468–475.
- 1081 Portin K, Vanni S, Virsu V, Hari R (1999) Stronger occipital cortical activation to lower
1082 than upper visual field stimuli. Neuromagnetic recordings. *Exp. Brain Res.*
1083 124:287–294.
- 1084 Price D, Tyler LK, Neto Henriques R, Campbell KL, Williams N, Treder MS, Taylor JR,
1085 Cam-CAN, Henson RNA (2017) Age-related delay in visual and auditory evoked
1086 responses is mediated by white- and grey-matter differences. *Nat. Commun.* 8:
1087 15671.
- 1088 Pumphrey RJ, Young JZ (1938) The rates of conduction of nerve fibres of various
1089 diameters in cephalopods. *J. Exp. Biol.* 15:453–466.
- 1090 Raz N, Levin N (2014) Cortical and white matter mapping in the visual system-more
1091 than meets the eye: on the importance of functional imaging to understand visual
1092 system pathologies. *Front. Integr. Neurosci.* 8:68.
- 1093 Rockland KS, Virga A (1989) Terminal arbors of individual “Feedback” axons projecting
1094 from area V2 to V1 in the macaque monkey: a study using immunohistochemistry
1095 of anterogradely transported Phaseolus vulgaris-leucoagglutinin. *J Comp Neurol.*
1096 285:54–72.
- 1097 Rockland KS (2020) What we can learn from the complex architecture of single
1098 axons. *Brain Struct. Funct.* [Epub ahead of print]

- 1099 Roebroek A, Miller KL, Aggarwal M (2019) Ex vivo diffusion MRI of the human brain:
1100 Technical challenges and recent advances. *NMR Biomed.* 32:e3941.
- 1101 Rokem A, Takemura H, Bock AS, Scherf KS, Behrmann M, Wandell BA, Fine I, Bridge
1102 H, Pestilli F (2017) The visual white matter: The application of diffusion MRI and
1103 fiber tractography to vision science. *J. Vis.* 17:4.
- 1104 Sachs H (1892) Das hemisphärenmark des menschlichen grosshirns. Leipzig: Verlag
1105 von georg thieme.
- 1106 Salmelin R, Hari R (1994) Spatiotemporal characteristics of sensorimotor
1107 neuromagnetic rhythms related to thumb movement. *Neuroscience* 60:537–550.
- 1108 Setsompop K, Cohen-Adad J, Gagoski BA, Raji T, Yendiki A, Keil B, Wedeen VJ, Wald
1109 LL (2012) Improving diffusion MRI using simultaneous multi-slice echo planar
1110 imaging. *NeuroImage* 63:569–580.
- 1111 Setsompop K, Fan Q, Stockmann J, Bilgic B, Huang S, Cauley SF, Nummenmaa A,
1112 Wang F, Rathi Y, Witzel T, Wald LL (2018) High-resolution in vivo diffusion
1113 imaging of the human brain with generalized slice dithered enhanced resolution:
1114 Simultaneous multislice (gSlider-SMS). *Magn. Reson. Med.* 79:141–151.
- 1115 Sherbondy AJ, Dougherty RF, Ben-Shachar M, Napel S, Wandell BA (2008a)
1116 ConTrack: finding the most likely pathways between brain regions using diffusion
1117 tractography. *J. Vis.* 8, 9:15.
- 1118 Sherbondy AJ, Dougherty RF, Napel S, Wandell BA (2008b) Identifying the human
1119 optic radiation using diffusion imaging and fiber tractography. *J. Vis.* 8, 10:12.
- 1120 Stikov N, Campbell JSW, Stroh T, Lavelée M, Frey S, Novak J, Nuara S, Ho M-K,
1121 Bedell BJ, Dougherty RF, Leppert IR, Boudreau M, Narayanan S, Duval T,
1122 Cohen-Adad J, Picard P-A, Gasecka A, Côté D, Pike GB (2015) In vivo histology
1123 of the myelin g-ratio with magnetic resonance imaging. *NeuroImage* 118:397–405.
- 1124 Takemura H, Ogawa S, Mezer AA, Horiguchi H, Miyazaki A, Matsumoto K, Shikishima
1125 K, Nakano T, Masuda Y (2019) Diffusivity and quantitative T1 profile of human
1126 visual white matter tracts after retinal ganglion cell damage. *NeuroImage*
1127 *Clin.* 23:101826.
- 1128 Takemura MY, Hori M, Yokoyama K, Hamasaki N, Suzuki M, Kamagata K, Kamiya K,
1129 Suzuki Y, Kyogoku S, Masutani Y, Hattori N, Aoki S (2017) Alterations of the optic
1130 pathway between unilateral and bilateral optic nerve damage in multiple sclerosis

- 1131 as revealed by the combined use of advanced diffusion kurtosis imaging and
1132 visual evoked potentials. *Magn. Reson. Imaging* 39:24–30.
- 1133 Taulu S, Simola J, Kajola M (2005) Applications of the signal space separation method.
1134 *IEEE Trans. Signal Process.* 53:3359–3372.
- 1135 Taulu S, Hari R (2009) Removal of magnetoencephalographic artifacts with temporal
1136 signal-space separation: demonstration with single-trial auditory-evoked
1137 responses. *Hum. Brain Mapp.* 30:1524–1534.
- 1138 Thurtell MJ, Bala E, Yaniglos SS, Rucker JC, Peachey NS, Leigh RJ (2009) Evaluation
1139 of optic neuropathy in multiple sclerosis using low-contrast visual evoked
1140 potentials. *Neurology* 73:1849–1857.
- 1141 Tournier JD, Calamante F, Connelly A (2012) MRtrix: Diffusion tractography in crossing
1142 fiber regions. *Int. J. Imaging Syst. Technol.* 22:53–66.
- 1143 Tzelepi A, Ioannides AA, Poghosyan V (2001) Early (N70m) neuromagnetic signal
1144 topography and striate and extrastriate generators following pattern onset
1145 quadrant stimulation. *NeuroImage* 13:702–718.
- 1146 Veraart J, Sijbers J, Sunaert S, Leemans A, Jeurissen B (2013) Weighted linear least
1147 squares estimation of diffusion MRI parameters: strengths, limitations, and pitfalls.
1148 *NeuroImage* 81:335–346.
- 1149 Vollmar C, O'Muircheartaigh J, Barker GJ, Symms MR, Thompson P, Kumari V,
1150 Duncan JS, Richardson MP, Koepp MJ (2010) Identical, but not the same:
1151 intra-site and inter-site reproducibility of fractional anisotropy measures on two 3.0
1152 T scanners. *NeuroImage* 51:1384–1394.
- 1153 Wagstyl K, Larocque S, Cucurull G, Lepage C, Cohen JP, Bludau S,
1154 Palomero-Gallagher N, Lewis LB, Funck T, Spitzer H, Dicksheid T, Fletcher PC,
1155 Romero A, Zilles K, Amunts K, Bengio Y, Evans AC (2020) BigBrain 3D atlas of
1156 cortical layers: cortical and laminar thickness gradients diverge in sensory and
1157 motor cortices. *PLoS Biol.* 18:e3000678.
- 1158 Wang L, Mruczek REB, Arcaro MJ, Kastner S (2015) Probabilistic maps of visual
1159 topography in human cortex. *Cereb. Cortex* 25:3911–3931.
- 1160 Waxman SG (1980) Determinants of conduction velocity in myelinated nerve fibers.
1161 *Muscle Nerve* 3:141–150.

- 1162 Weiskopf N, Mohammadi S, Lutti A, Callaghan MF (2015) Advances in MRI-based
1163 computational neuroanatomy: from morphometry to in-vivo histology. *Curr. Opin.*
1164 *Neurol.* 28:313–322.
- 1165 Yeatman JD, Dougherty RF, Myall NJ, Wandell BA, Feldman HM (2012) Tract profiles
1166 of white matter properties: automating fiber-tract quantification. *PLoS One*
1167 7:e49790.
- 1168 Yoshida F, Hirata M, Onodera A, Goto T, Sugata H, Yorifuji S (2017) Noninvasive
1169 spatiotemporal imaging of neural transmission in the subcortical visual pathway.
1170 *Sci. Rep.* 7:4424.
- 1171 Zhang H, Schneider T, Wheeler-Kingshott CA, Alexander DC (2012) NODDI: practical
1172 in vivo neurite orientation dispersion and density imaging of the human brain.
1173 *NeuroImage* 61:1000–1016.
1174

